Chemical Engineering Journal 435 (2022) 134946

Contents lists available at ScienceDirect

Chemical Engineering Journal

journal homepage: www.elsevier.com/locate/cej

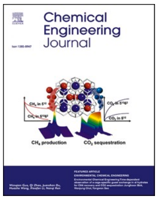

Kinetic modelling of the methanol synthesis from CO_2 and H_2 over a CuO/CeO_2/ZrO_2 catalyst: The role of CO_2 and CO hydrogenation

Serena Poto [a], Damian Vico van Berkel [a], Fausto Gallucci [a,b], M. Fernanda Neira d'Angelo [a,*]

[a] Sustainable Process Engineering, Chemical Engineering and Chemistry, Eindhoven University of Technology, De Rondom 70, 5612 AP, Eindhoven, The Netherlands
[b] Eindhoven Institute for Renewable Energy Systems (EIRES), Eindhoven University of Technology, PO Box 513, Eindhoven 5600 MB, The Netherlands

ARTICLE INFO

Keywords:
CO_2 conversion
Methanol synthesis
Kinetic modelling
Oxygen vacancies
Cerium-zirconium oxides

ABSTRACT

This work addresses the kinetics of the CO_2 hydrogenation to methanol over a Cu/CeO_2/ZrO_2 catalyst studied using single-site, dual-sites and three adsorption sites kinetic models. Physicochemical constraints and statistical indicators are used as tool for model discrimination. The best performing model is used to elucidate the reaction mechanism and the relative roles of the Cu-sites and oxygen vacancies. The results show that the dissociative adsorption of H_2 occurs on the Cu^0 sites, while CO_2 is attracted to the oxygen vacancies created by the CeO_2-ZrO_2 solid solution. Then, the adsorbed H interacts preferentially with the carbon atom, favouring the so-called "formate" route. The CO formed via the r-WGS reaction could either desorb to the gas phase or react via hydrogenation to methanol. Analysis of the relative contributions of the CO_2 and CO hydrogenation (i.e. direct and indirect pathways, respectively) to the methanol synthesis reveals that the latter is in fact preferential at high temperatures (i.e. about 100% of methanol is produced from CO at 260 °C and 30 bar), and it shows an optimum vs the H_2:CO_2 ratio (c.a. 7 at 200 °C and 30 bar), which corresponds to the saturation of the Cu^0 sites with H_2. Thus, this work provides an essential tool (i.e., kinetic model) for the design of reactors and processes based on novel catalysts, and importantly, it offers a deeper understanding of the reaction mechanism as basis for further catalyst development.

1. Introduction

The combustion of hydrocarbons to produce energy entails a critical global challenge that needs to be tackled with urgency. The usage of fossil fuels correlates directly to the release of greenhouse gasses – especially CO_2 – into the atmosphere, which is the main responsible of global warming [1,2]. Hence, in the last century research has been focusing on the development of carbon capture and storage technologies (CCS) first and, more recently, on the alternatives for CO_2 utilization (CCU) [3–6]. An interesting approach for CCU is the CO_2 reduction with renewable H_2 to produce valuable chemicals and/or energy carriers [7]. In this context, the CO_2 conversion to methanol is particularly appealing due to the high methanol demand worldwide (i.e. about 200 kton of methanol are used every day as chemical feedstock and transportation fuel) [8]. Indeed, methanol could be used directly as an alternative fuel or as intermediate for the production of dimethyl ether, olefins, gasoline and aromatics [9–11]. The CO_2 hydrogenation to methanol is a catalytic gas phase process which follows three main reactions: the direct hydrogenation of CO_2 to methanol (reaction 1), the production of CO through the r-WGS reaction (reaction 2) and the hydrogenation of CO to methanol (reaction 3).

CO_2 hydrogenation: $CO_2+3H_2 \rightleftarrows CH_3OH + H_2O \; \Delta H_0=-49.5$ kJ/mol (1)

Reverse water gas shift: $CO_2+H_2 \rightleftarrows CO+H_2O \; \Delta H_0=+41.2$ kJ/mol (2)

CO hydrogenation: $CO+2H_2 \rightleftarrows CH_3OH \; \Delta H_0=-90.5$ kJ/mol (3)

Among these reactions, the CO_2 hydrogenation to methanol is the most desired. Inevitably, the r-WGS takes place in parallel, accelerating the H_2 depletion and, at the same time, contributing to the production of water. As a matter of fact, water is the main reaction by-product, which limits the system thermodynamically and causes catalyst deactivation [12]. Depending on the catalyst, the CO hydrogenation to methanol (reaction 3) could take place simultaneously, partially balancing the negative effect of the r-WGS. Nowadays, methanol is produced industrially from syngas feedstock (i.e., mixture of CO, H_2 and c.a. 3% of CO_2) at pressures of 50–80 bar and temperatures of 200–300 °C, over CuO/ZnO/Al_2O_3 catalytic beds [13,14]. Since the benchmark technology involves only traces of CO_2 in the feedstock [15], the corresponding

---

* Corresponding author.
E-mail address: M.F.Neira.dAngelo@tue.nl (M. Fernanda Neira d'Angelo).

https://doi.org/10.1016/j.cej.2022.134946
Received 21 November 2021; Received in revised form 18 January 2022; Accepted 24 January 2022

Nomenclature

Symbol, Definition, Units

S_{Cu}	Copper surface area, ($m^2_{Cu}\cdot g^{-1}$)
N_{av}	Avogadro' s number, ($-$)
M_{Cu}	Copper molecular weight, ($g\cdot mol^{-1}$)
D_{Cu}	Copper dispersion, (%)
d^{SV}_{Cu}	Average surface-volume copper diameter, (nm)
ρ_{Cu}	Copper density, ($g\cdot m^{-3}_{Cu}$)
X, Y	H_2 consumption from 1st and 2nd TPR, respectively, ($mL_{H_2}\cdot g^{-1}_{cat}$)
d_{Cu}	Copper crystallite dimension from XRD, (nm)
ρ_{cat}	Catalyst solid density, ($kg\cdot m^{-3}_{cat,s}$)
$\rho_{b,cat}$	Catalyst apparent density, ($kg\cdot m^{-3}_{cat}$)
ε_{cat}	Catalyst porosity, ($m^3_{pores}\cdot m^{-3}_{cat}$)
S_{BET}	BET surface area, ($m^2\cdot g^{-1}$)
$P.V.$	Pore volume, ($cm^3\cdot g^{-1}$)
$P.D.$	Pore diameter, (nm)
GHSV	Gas hourly space velocity, ($NL\cdot kg^{-1}_{cat}\cdot h^{-1}$)
X_{CO_2}	CO_2 conversion, (%)
Y_i	Yield of product i, (%)
STY_i	Space time yield of product i, ($mmol\cdot h^{-1}\cdot g^{-1}_{cat}$)
S_i	Selectivity of product i, (%)
w_{cat}	Catalyst weight, (kg)
F_i	Molar flow rate of component i, ($mol\cdot s^{-1}$)
y_i	Molar fraction of component i, ($-$)
$RMSE_i$	Root mean square error of component i, ($-$)
OF	Objective function, ($-$)
N_{data}	Number of experimental data, ($-$)
ϕ_o	Inlet volumetric flow rate, ($NL\cdot h^{-1}$)
T	Temperature, (K)
P	Total pressure, (bar)
ν_{ji}	Stoichiometric number of component i in reaction j, ($-$)
r_j	Rate of reaction j, ($mol\cdot s^{-1}\cdot kg^{-1}_{cat}$)
N_r	Total number of reaction, ($-$)
k_j	Kinetic constant of reaction j, ($mol\cdot s^{-1}\cdot kg^{-1}_{cat}$)
$k_{j,0}$	Pre-exponential factor of the kinetic constant of reaction j, (depending on model)
b_i	Adsorption constant of component i, (depending on model)
K^{eq}_j	Equilibrium constant of reaction j, (depending on reaction)
$\Delta H^0_{ads,i}$	Standard enthalpy of adsorption of component i, ($J\cdot mol^{-1}$)
$\Delta S^0_{ads,i}$	Standard entropy of adsorption of component i, ($J\cdot mol^{-1}\cdot K^{-1}$)
$E_{a,j}$	Activation energy of reaction j, ($J\cdot mol^{-1}$)
R	Gas constant, ($J\cdot mol^{-1}\cdot K^{-1}$)
Ca	Carberry's number, ($-$)
Da_{II}	Second Damkohler number, ($-$)
D_e	Effective diffusivity, ($m^2\cdot s^{-1}$)
$r_{i,obs,V}$	Observed reaction rate per volume of catalyst, ($mol\cdot s^{-1}\cdot m^{-3}_{cat}$)
n_i	Order of reaction with respect to component i, ($-$)
k_{gs}	Gas-solid mass transfer coefficient, ($m\cdot s^{-1}$)
r^+_i	Forward rate of reaction of component i, ($mol\cdot s^{-1}\cdot kg^{-1}_{cat}$)
c_{ib}	Concentration of species i in the bulk phase, ($mol\cdot m^{-3}$)
c_{is}	Concentration of species i on the catalyst surface, ($mol\cdot m^{-3}$)
$F_{statistic}$	Statistic indicator of the F-test, ($-$)
$F_{critical}$	Critical value of F-, from Fisher distribution tables, ($-$)
s^2_1	Variance of the lack of fit, ($-$)
s^2_2	Variance of the experimental error, ($-$)
N_{var}	Number of variables (parameters of kinetic models), ($-$)
p_i	Partial pressure of component i, (bar)
β	Adsorption term of Bussche and Froment kinetic model, ($-$)
Θ_1, Θ_2	Adsorption terms of Graaf's kinetic model, ($bar^{-0.5}$)
$\Theta^{\odot}, \Theta^{*}, \Theta^{\otimes}$	Adsorption terms of Seidel's kinetic model, ($-$)
ϕ	Total amount of reduced centers, ($-$)
$\frac{\gamma_*}{\gamma_0}$	Relative contact free energy of Cu and CeZr, ($-$)

Subscripts and Superscript

0	Inlet reactor condition
1	CO_2 hydrogenation to methanol reaction
2	Reverse water gas shift reaction
3	CO hydrogenation to methanol reaction
exp	Experimental value
$calc$	Calculated value

catalyst is not necessarily optimal when using pure CO_2, i.e., a thermodynamically very stable molecule, as the sole carbon source. Usually CO_2 adsorption is not strong enough [16] and efforts are required specifically on novel catalyst formulations [17]. Over the years, researchers have proposed a variety of different catalysts for the CO_2 hydrogenation to methanol, with particular focus on Cu-based systems, in combination with different metal oxides as carrier and/or promoters [18–21]. First, important research efforts aimed at replacing the hydrophilic Al_2O_3 support, which could deactivate in presence of the large amounts of water produced in all the reactions [22]. In most of the catalyst formulations, the ZnO oxide still acts as main promoter, since it guarantees both a higher Cu dispersion and the formation of $Cu^{\delta+}$ sites at the Cu-ZnO interface [23–25]. On the other hand, various carriers/promoters have been proposed in literature such as ZrO_2 [17,25–29], CeO_2 [22,30–34], Fe_2O_3 [34–36], SiO_2 [37–39], and TiO_2 [30,40–43]. Most recently, the synergistic effect of CeO_2-ZrO_2 mixed oxides has received particular attention due to their high redox ability, improved thermal stability [44] and superior oxygen storage capacity (OCS) [45], properties that have proved highly beneficial for different reactive systems, such as the oxidation of aliphatic C2 [46], the conversion of NOx [47], the reduction of NO by propene [48] and, most recently, for the CO_2 hydrogenation to methanol [49–51]. The introduction of smaller Zr^{4+} ions into the CeO_2 tetrahedron creates a defective fluorite structure, which facilitates the adsorption of oxygen [52]. Shi et al., [49] proposed for the first time a ternary $CuO/CeO_2/ZrO_2$ catalyst for the CO_2 hydrogenation to methanol. They found that a Ce:Zr mass ratio of 1 optimizes the basicity of the system in favour of the CO_2 adsorption capacity. Their $Cu_{30}Ce_{35}Zr_{35}O$ catalyst showed excellent reducibility and Cu dispersion, as well as a balanced distribution of Cu^0 and strong basic sites to enhance the H_2 dissociative-adsorption and the formation of the H_2CO intermediate, which preferentially hydrogenates to form methanol. Wang et al., [50] investigated the reaction pathway via *in situ* DRIFTS analysis. They showed that a calcination temperature of 450 °C increases the CuO surface area and the formation of Cu-Ce-Zr sites, which favour the formation of H* and bi/m-HCOO*, responsible for the high selectivity to methanol.

In any catalytic process, kinetic modelling is an essential tool to support efforts on catalyst development, to elucidate reaction mechanisms as well as to aid reactor design and process optimization. Numerous kinetic models have been proposed over the years to describe the methanol synthesis, mostly on commercial catalysts [13,53–57]. However, the majority of the kinetic models trace back to the works of Graaf et al., [58] and Bussche and Froment [59]. Both models propose a Langmuir-Hinshelwood-Hougen-Watson (LHHW) mechanism with the dissociative adsorption of H_2. Graaf et al., established a dual-sites mechanism (i.e., one for CO and CO_2 and one for H_2O and H_2) where methanol is produced from CO_2 and CO simultaneously. On the contrary, Bussche and Froment considered a mechanism where Cu is the sole active site and CO_2 is the only carbon source for the methanol production. Even today, literature shows disagreements on the relative contribution of CO and CO_2 to the methanol synthesis. For example, Liu et al., [60] propose at least four parallel reactions: CO-CO_2 exchange, CO hydrogenation, CO_2 hydrogenation and WGS, while Bowker et al., [61] proposed that CO_2 is the only responsible of methanol synthesis, even when feeding CO/CO_2/H_2 mixtures. Interestingly, Yang et al., [62] proved that the CO_2 and CO contributions to methanol synthesis varies with the operating conditions. More recently, Niels et al., [63] found that CO_2 is the immediate source for methanol (i.e., CO_2 pathway is one order of magnitude faster), whereas the presence of CO is inhibitory at low conversion due to competitive adsorption, and beneficial at higher conversion due to the removal of water via the WGS. Finally, L.C. Grabow and M. Mavrikakis [64] showed through DFT calculations that about 2/3 of the methanol comes from CO_2 in the conventional process (i.e., syngas feed). However, the situation could be completely different with CO_2-rich streams and other catalyst formulations.

More recently, Park et al., [65] developed a model considering three-sites adsorption, where CO_2 and CO adsorb on two distinct sites. In this study the authors carried out a rate determining step analysis (RDS) based on the mechanistic hypotheses earlier proposed by Graaf et al., to find the rate expressions that best fit the experimental data. Seidel et al., [56] reviewed the elementary steps involved in the three-sites adsorption mechanism, proposing an even more complex kinetic model. This was recently simplified by Slotboom et al., [66], who reduced the number of kinetic parameters considerably.

Despite the extensive literature database of kinetic models and rate expressions for the Cu:ZnO system supported on either Al_2O_3 (i.e., benchmark formulation) or other metal oxides, kinetic modelling of the methanol synthesis remains an intriguing research topic, with at least two important open questions: 1) what are the type and number of the catalyst active sites involved in the methanol synthesis; and 2) which is the dominant C-source for methanol formation (i.e., CO/CO_2) and the corresponding prevailing reaction pathway. In addition, and to the best of our knowledge, the kinetics of this reaction on novel catalysts such as Cu-Ce-Zr mixed oxides (i.e., better performant catalysts for the conversion of CO_2) has not been investigated yet.

Herein, the kinetic model of methanol synthesis from CO_2 and H_2 over a Cu-Ce-Zr mixed oxide catalyst is investigated by means of an RDS analysis for the single-site, dual-site and three-sites adsorption kinetic model, based on the most relevant mechanistic hypotheses retrieved from literature. A total of 6 kinetic models are compared with a complete set of 96 experimental data in the range of temperature, pressure, H_2:CO_2 molar ratio and GHSV of 200–260 °C and 10–40 bar, 3–7 and 7500–24000 $NL\cdot kg_{cat}^{-1}\cdot h^{-1}$, respectively.

The preparation of the ternary catalyst according to the works of Shi et al., [49] and Wang et al., [50] is followed by in depth catalyst characterization and extensive kinetic tests. Statistical analysis of the data combined with physicochemical constraints are used as tool for model discriminations. This work pays particular attention to the relative contribution of CO_2 and CO to the formation of methanol (i.e., methanol synthesis from direct and indirect route, respectively) under various reaction conditions, by means of a theoretical differential analysis. The identification of the kinetic model, together with a detailed analysis of the reaction rates and the interplay between CO_2 and CO hydrogenation will lead to a better understanding of this system. In this study, we will gain insights into the reaction mechanisms, identify the active sites and their role within the methanol formation, which is key for further improvement of this catalyst formulation, as well as an essential tool for reactor and process design.

2. Kinetic models for methanol synthesis: State of the art

To elucidate on the reaction pathway involved in the CO_2 hydrogenation to methanol over a copper-cerium-zirconium mixed oxides catalyst, the most relevant kinetic models reported in literature have been explored and re-parametrized. All the available kinetic models can be sorted in three groups, based on the number of active sites considered in the formulation of the mechanism. A detailed discussion is given below.

2.1. Single-site adsorption mechanism

The most relevant kinetic model considering a single-site adsorption mechanism is the one developed by Bussche and Froment in 1996 [59]. The most important assumption is that CO_2 is the sole carbon source for methanol synthesis. As a result, only reaction (1) and (2) take place on the Cu surface of the catalyst, where both H_2 and CO_2 undergo dissociative adsorption. According to the authors, the rate determining steps are: 1) the CO_2 dissociation on the active sites, which releases surface oxygen for the rWGS reaction and 2) the hydrogenation of the formate species for the CO_2 hydrogenation to methanol. The rate equations are reported in Eq. 3–5.

$$r_1 = k_1 p_{CO_2} p_{H_2}\left(1 - \frac{1}{K_1^{eq}}\frac{p_{H_2O}p_{CH_3OH}}{p_{H_2}^3 p_{CO_2}}\right)\beta^3 \tag{3}$$

$$r_2 = k_2 p_{CO_2}\left(1 - \frac{1}{K_2^{eq}}\frac{p_{H_2O}p_{CO}}{p_{H_2}p_{CO_2}}\right)\beta \tag{4}$$

$$\beta = \left(1 + b_{H_2O/H_2/8/9}\frac{p_{H_2O}}{p_{H_2}} + b_{H_2}p_{H_2}^{0.5} + b_{H_2O}p_{H_2O}\right)^{-1} \tag{5}$$

The Bussche and Froment model considers three adsorption constants (i.e., $b_{H_2O/H_2/8/9}$, b_{H_2} and b_{H_2O}) and two kinetic constants (i.e., k_1 and k_2), for a total of 10 parameters to be optimized.

2.2. Dual-site adsorption mechanism

The most important and widely employed kinetic model describing the methanol synthesis is the model developed by Graaf et al., [58] in 1988. In their first publication, the authors had already recognized the lack of agreement in the literature on whether the carbon source for the methanol production is CO or CO_2. As a result, they developed a model including both pathways (reaction 1, 2 and 3). All the reactions are assumed to be based on a dual-site LHHW mechanism, where CO and CO_2 adsorb competitively on one site (s_1) and H_2 and H_2O adsorb competitively on a second site (s_2), with dissociation of H_2. The adsorption of methanol is once again neglected. The rate equations are reported in Eq. 6–8, with the two adsorption terms (i.e., Θ_1 and Θ_2) related to the site s_1 and site s_1 described in Eq. 9–10.

$$r_1 = k_1 b_{co_2} C \Theta_1 \Theta_2 \tag{6}$$

$$r_2 = k_2 b_{co_2} B \Theta_1 \Theta_2 \tag{7}$$

$$r_3 = k_3 b_{co} A \Theta_1 \Theta_2 \tag{8}$$

$$\Theta_1 = \left(1 + b_{co}p_{co} + b_{CO_2}p_{CO_2}\right)^{-1} \tag{9}$$

$$\Theta_2 = \left(p_{H_2}^{0.5} + \frac{b_{H_2O}}{\sqrt{b_{H_2}}}p_{H_2O}\right)^{-1} \tag{10}$$

where A, B, and C represents the driving force of the CO hydrogenation, r-WGS and CO_2 hydrogenation to methanol, respectively. As a matter of fact, the authors provided also different expressions for the driving forces terms, which depends on the particular RDS for the specific reaction. All the (48) combinations are reported in Table 1 and were tested in this study.

The model from Graaf et al., includes 3 kinetic constants (i.e., k_1, k_2 and k_3) and 3 adsorption constants (i.e., b_{co}, b_{CO_2} and $\frac{b_{H_2O}}{\sqrt{b_{H_2}}}$), for a total of 12 kinetic parameters.

More recently, Henkel modified the model developed by Graaf et al., excluding the CO hydrogenation to methanol [54]. His reparameterization was based on two sets of experimental results, obtained from two distinct set-ups: 1) a Berty reactor and 2) a micro-fixed bed reactor, from which he obtained two different set of kinetic parameters [55]. The rate equations proposed for the CO_2 hydrogenation and the rWGS are reported in Eq. 11–12, which lead to a total of 10 kinetic parameters.

$$r_1 = \frac{k_1 b_{CO_2} p_{co_2} p_{H_2}^{1.5}\left(1 - \frac{p_{CH_3OH}p_{H_2O}}{p_{CO_2} p_{H_2}^3 K_1^{eq}}\right)}{\left(1 + b_{co}p_{co} + b_{CO_2}p_{CO_2}\right)\left(p_{H_2}^{0.5} + b_{H_2O/H_2}p_{H_2O}\right)} \tag{11}$$

$$r_2 = \frac{k_2 b_{CO_2} p_{co_2} p_{H_2}\left(1 - \frac{p_{CO}p_{H_2O}}{p_{CO_2} p_{H_2} K_2^{eq}}\right)}{\left(1 + b_{co}p_{co} + b_{CO_2}p_{CO_2}\right)\left(p_{H_2}^{0.5} + b_{H_2O/H_2}p_{H_2O}\right)} \tag{12}$$

2.3. *Three-sites adsorption mechanism*

In 2014, Park et al., [65] proposed a reaction pathway, based on the mechanism developed by Graaf et al., with the introduction of a third adsorption site exclusively for CO_2. The authors considered the methanol dehydration to dimethyl ether in their reaction scheme, which was discarded in our analysis since no traces of DME were detected during the experimentation. The rate equations are summarized in Eq. 13–15. The model from Park et al., involves 14 kinetic parameters to be optimized.

$$r_1 = \frac{k_1 b_{CO_2}\left(p_{co_2} p_{H_2}^{1.5} - \frac{p_{CH_3OH}p_{H_2O}}{p_{H_2}^{1.5} K_1^{eq}}\right)}{\left(1 + b_{CO_2}p_{CO_2}\right)\left(1 + b_{H_2}^{0.5}p_{H_2}^{0.5} + b_{H_2O}p_{H_2O}\right)} \tag{13}$$

$$r_2 = \frac{k_2 b_{CO_2}\left(p_{co_2} p_{H_2} - \frac{p_{CO}p_{H_2O}}{K_2^{eq}}\right)}{\left(1 + b_{CO_2}p_{CO_2}\right)\left(1 + b_{H_2}^{0.5}p_{H_2}^{0.5} + b_{H_2O}p_{H_2O}\right)} \tag{14}$$

$$r_3 = \frac{k_3 b_{CO}\left(p_{co} p_{H_2}^{1.5} - \frac{p_{CH_3OH}}{p_{H_2}^{0.5} K_3^{eq}}\right)}{\left(1 + b_{CO}p_{CO}\right)\left(1 + b_{H_2}^{0.5}p_{H_2}^{0.5} + b_{H_2O}p_{H_2O}\right)} \tag{15}$$

Table 1
Expressions of the driving force terms for reaction 1, 2 and 3 according to the rate determining steps (RDS) *A*, *B* and *C* provided by Graaf et al.,

RDS	Driving force
A_1: $COs_1 + Hs_2 \rightleftarrows HCOs_1 + s_2$	$p_{co}p_{H_2}^{0.5} - p_{CH_3OH}/p_{H_2}^{1.5}K_3^{eq}$
A_2: $HCOs_1 + Hs_2 \rightleftarrows H_2COs_1 + s_2$	$p_{co}p_{H_2} - p_{CH_3OH}/p_{H_2}K_3^{eq}$
A_3: $H_2COs_1 + Hs_2 \rightleftarrows H_3COs_1 + s_2$	$p_{co}p_{H_2}^{1.5} - p_{CH_3OH}/p_{H_2}^{0.5}K_3^{eq}$
A_4: $H_3COs_1 + Hs_2 \rightleftarrows CH_3OH + s_1 + s_2$	$p_{co}p_{H_2}^{2} - p_{CH_3OH}/K_3^{eq}$
B_1: $CO_2s_1 + Hs_2 \rightleftarrows HCO_2s_1 + s_2$	$p_{co_2}p_{H_2}^{0.5} - p_{CO}p_{H_2O}/p_{H_2}^{0.5}K_2^{eq}$
B_2: $HCO_2s_1 + Hs_2 \rightleftarrows COs_1 + H_2Os_2$	$p_{co_2}p_{H_2} - p_{CO}p_{H_2O}/K_2^{eq}$
C_1: $CO_2s_1 + Hs_2 \rightleftarrows HCO_2s_1 + s_2$	$p_{co_2}p_{H_2}^{0.5} - p_{CH_3OH}p_{H_2O}/p_{H_2}^{2.5}K_1^{eq}$
C_2: $HCO_2s_1 + Hs_2 \rightleftarrows H_2CO_2s_1 + s_2$	$p_{co_2}p_{H_2} - p_{CH_3OH}p_{H_2O}/p_{H_2}^{2}K_1^{eq}$
C_3: $H_2CO_2s_1 + Hs_2 \rightleftarrows H_3CO_2s_1 + s_2$	$p_{co_2}p_{H_2}^{1.5} - p_{CH_3OH}p_{H_2O}/p_{H_2}^{1.5}K_1^{eq}$
C_4: $H_3CO_2s_1 + Hs_2 \rightleftarrows H_2COs_1 + H_2Os_2$	$p_{co_2}p_{H_2}^{2} - p_{CH_3OH}p_{H_2O}/p_{H_2}K_1^{eq}$
C_5: $H_2COs_1 + Hs_2 \rightleftarrows H_3COs_1 + s_2$	$p_{co_2}p_{H_2}^{2.5}/p_{H_2O} - p_{CH_3OH}/p_{H_2}^{0.5}K_1^{eq}$
C_6: $H_3COs_1 + Hs_2 \rightleftarrows CH_3OH + s_1 + s_2$	$p_{co_2}p_{H_2}^{3}/p_{H_2O} - p_{CH_3OH}/K_1^{eq}$

Few years later, in 2018, Seidel et al., [56] developed an even more detailed model based on three adsorption sites, reviewing also the elementary reactions involved and the rate determining step of each reaction. The active sites are distinguished as follows:

$\odot$ for oxidized surface centers, assumed as active center for CO hydrogenation

$\ast$ for reduced surface centers, assumed as active center for CO_2 hydrogenation

$\otimes$ as the active surface center for the decomposition of H_2

The rate expressions are reported in Eq. 16–18 with the corresponding adsorption terms in Eq. 19–21.

$$r_1 = \phi^2 k_1 p_{CO_2} p_{H_2}^2 \left(1 - \frac{p_{CH_3OH}p_{H_2O}}{p_{CO_2}p_{H_2}^3 K_1^{eq}}\right)\Theta^{\ast 2}\Theta^{\otimes 4} \tag{16}$$

$$r_2 = \left(\frac{\phi}{1-\phi}\right) k_2 p_{CO_2}\left(1 - \frac{p_{CO}p_{H_2O}}{p_{CO_2}p_{H_2}K_2^{eq}}\right)\Theta^{\ast}\Theta^{\odot} \tag{17}$$

$$r_3 = (1-\phi) k_3 p_{CO} p_{H_2}^2 \left(1 - \frac{p_{CH_3OH}}{p_{CO}p_{H_2}^2 K_3^{eq}}\right)\Theta^{\odot}\Theta^{\otimes 4} \tag{18}$$

$$\Theta^{\odot} = \left(1 + b_{CO}p_{CO}\right)^{-1} \tag{19}$$

$$\Theta^{\ast} = \left(1 + \frac{b_{H_2O}b_O}{b_{H_2}}\frac{p_{H_2O}}{p_{H_2}} + b_{CO_2}p_{CO_2} + b_{H_2O}p_{H_2O}\right)^{-1} \tag{20}$$

$$\Theta^{\otimes} = \left(1 + \sqrt{b_{H_2}}\, p_{H_2}^{0.5}\right)^{-1} \tag{21}$$

The parameter ϕ represents the total amount of reduced center, while $(1-\phi)$ represents the number of oxidized centers. Slootbom et al., [66] have recently corrected the definition of ϕ, assuming a maximum coverage of the reduced center of 90% (Eq. 22).

$$\phi = \phi_w - 0.1 \tag{22}$$

The authors used the relation of Ovesen et al., [67] for the calculation of ϕ_w, as follows:

$$\phi_w = \frac{1}{2}\left(1 - \frac{\gamma_*}{\gamma_0}\right) \tag{23}$$

where $\frac{\gamma_*}{\gamma_0}$ is the relative contact free energy of Cu and Zn, for the benchmark formulation, and of Cu and the CeZr solution for our system. The $\frac{\gamma_*}{\gamma_0}$ ratio is calculated according to Eq. 24–25, with the introduction of a new kinetic parameter (ΔG_3).

$$\frac{\gamma_*}{\gamma_0} = \frac{1 - \sqrt{K_3 \frac{p_{H_2}p_{CO}}{p_{H_2O}p_{CO_2}}}}{1 + \sqrt{K_3 \frac{p_{H_2}p_{CO}}{p_{H_2O}p_{CO_2}}}} \tag{24}$$

$$K_3 = \exp\left(\frac{\Delta G_3}{RT}\right) \tag{25}$$

In this model, the adsorption constant dependency on temperature is neglected. This lead to a total of 12 parameters, if the $\frac{b_{H_2O}b_O}{b_{H_2}}$ group is parametrized as a single constant.

In 2020 Slotboom et al., [66] simplified the three-sites model, drastically reducing the amount of parameters (i.e., 6 in the simplified version). The authors revisited the elementary reaction steps of Bussche and Froment, thus, considering only CO_2 as the carbon source for methanol production, with the updates from recent literature. As Graaf et al., proposed in their study for the dual-sites adsorption mechanism, Slotboom et al., provided a tool for identifying the rate determining step for both the CO_2 hydrogenation and the rWGS (i.e., the CO hydrogenation is neglected). All the possible rate expressions are summarized in Table 2, with a total of 30 kinetic models, with 6 parameters each. The adsorption term, $\theta^{\ast}$, is defined by Eq. 26.

Table 2

Rate determining step for the CO_2 hydrogenation and rWGS reaction and the corresponding rate expression adapted from Slotboom et al., [66].

RDS	Driving force
2: $CO_2 + 2\divideontimes + H\otimes \rightleftarrows HCO_2\divideontimes\divideontimes$	$r_1 = k_1 p_{CO_2} p_{H_2}\left(1 - \frac{p_{CH_3OH} p_{H_2O}}{p_{CO_2} p_{H_2}^3 K_1^{eq}}\right)\theta^{\divideontimes 2}$
3: $HCO_2\divideontimes\divideontimes + H\otimes \rightleftarrows HCOOH\divideontimes\divideontimes + \otimes$	$r_1 = k_1 p_{CO_2} p_{H_2}^{1.5}\left(1 - \frac{p_{CH_3OH} p_{H_2O}}{p_{CO_2} p_{H_2}^3 K_1^{eq}}\right)\theta^{\divideontimes 2}$
4: $HCOOH\divideontimes\divideontimes \rightleftarrows HCO\divideontimes + OH\divideontimes$	$r_1 = k_1 p_{CO_2} p_{H_2}^{2}\left(1 - \frac{p_{CH_3OH} p_{H_2O}}{p_{CO_2} p_{H_2}^3 K_1^{eq}}\right)\theta^{\divideontimes 2}$
5: $HCO\divideontimes + H\otimes \rightleftarrows H_2CO\divideontimes + \otimes$	$r_1 = k_1 p_{CO_2} p_{H_2}^{1.5}\left(1 - \frac{p_{CH_3OH} p_{H_2O}}{p_{CO_2} p_{H_2}^3 K_1^{eq}}\right)\theta^{\divideontimes}$
6: $H_2CO\divideontimes + H\otimes \rightleftarrows H_3CO\divideontimes + \otimes$	$r_1 = k_1 p_{CO_2} p_{H_2}^{2}\left(1 - \frac{p_{CH_3OH} p_{H_2O}}{p_{CO_2} p_{H_2}^3 K_1^{eq}}\right)\theta^{\divideontimes}$
7: $H_3CO\divideontimes + H\otimes \rightleftarrows CH_3OH + \divideontimes + \otimes$	$r_1 = k_1 p_{CO_2} p_{H_2}^{2.5}\left(1 - \frac{p_{CH_3OH} p_{H_2O}}{p_{CO_2} p_{H_2}^3 K_1^{eq}}\right)\theta^{\divideontimes}$
rWGS with CO_2 dissociation	
11: $CO_2 + \divideontimes \rightleftarrows CO_2\divideontimes$	$r_2 = k_2 p_{CO_2} p_{H_2}^{0.5}\left(1 - \frac{p_{CO} p_{H_2O}}{p_{CO_2} p_{H_2} K_2^{eq}}\right)\theta^{\divideontimes}$
12: $CO_2\divideontimes + \odot \rightleftarrows CO\odot + O\divideontimes$	Equal to 11
13: $CO\odot \rightleftarrows CO + \odot$	$r_2 = k_2 p_{CO_2}\left(1 - \frac{p_{CO} p_{H_2O}}{p_{CO_2} p_{H_2} K_2^{eq}}\right)$
rWGS with COOH decomposition	
14: $CO_2\divideontimes + H\otimes \rightleftarrows COOH\divideontimes + \otimes$	Equal to 11
15: $COOH\divideontimes + \odot \rightleftarrows CO\odot + OH\divideontimes$	$r_2 = k_2 p_{CO_2} p_{H_2}\left(1 - \frac{p_{CO} p_{H_2O}}{p_{CO_2} p_{H_2} K_2^{eq}}\right)\theta^{\divideontimes}$
rWGS with $\divideontimes$ and $\odot$ similar sites	
16: $CO_2\divideontimes + \divideontimes \rightleftarrows CO\divideontimes + O\divideontimes$	$r_2 = k_2 p_{CO_2} p_{H_2}\left(1 - \frac{p_{CO} p_{H_2O}}{p_{CO_2} p_{H_2} K_2^{eq}}\right)\theta^{\divideontimes 2}$
17: $CO\divideontimes \rightleftarrows CO + \divideontimes$	Equal to 11
18: $COOH\divideontimes + \divideontimes \rightleftarrows CO\divideontimes + OH\divideontimes$	$r_2 = k_2 p_{CO_2} p_{H_2}^{1.5}\left(1 - \frac{p_{CO} p_{H_2O}}{p_{CO_2} p_{H_2} K_2^{eq}}\right)\theta^{\divideontimes 2}$

$$\theta^{\divideontimes} = \left(b_{H_2} p_{H_2}^{0.5} + b_{H_2O/9} p_{H_2O} + p_{CH_3OH}\right)^{-1} \tag{26}$$

3. Experimental

3.1. Catalyst synthesis and characterization

The Cu-Ce-Zr mixed oxides catalyst was prepared with a CuO loading of 50 wt%, to be comparable to the benchmark formulation, and a CeO_2:ZrO_2 mass fraction of 1, as recently optimized by Shi et al., [49]. The catalyst was synthesized via the gel-oxalate coprecipitation method [27]. The required amount of metal nitrate precursors (i.e., $Cu(NO_3)_2{\cdot}2.5H_2O$, $Ce(NO_3)_3{\cdot}6H_2O$ and $ZrO(NO_3)_2{\cdot}6H_2O$) were solubilized in ethanol and coprecipitated by adding an oxalic acid solution (20 wt% excess) dropwise, at room temperature and under continuous stirring. The precipitate was stirred for 3 h, aged overnight, centrifuged and washed with deionized water, dried at 95 °C for 16 h and calcined at 450 °C for 4 h. The catalyst was pelletized, crushed and sieved to produce 50–125 μm particle size, to be used for the characterization techniques and reaction tests. The chemical composition of the synthesized catalyst was measured via microwave plasma atomic emission spectroscopy, using an Agilent MP-AES 4200 elemental analyzer. Prior to the analysis, about 0.1 g of catalyst sample was digested in 70 v.% HNO_3 solution at 80 °C overnight and then diluted with 5 v.% HNO_3 solution (i.e., blank solution), to reach ppm values of the metal content. The specific surface area (S.A.) and pore volume (P.V.) were determined via the BET and BJH elaboration of the N_2 adsorption–desorption isotherms at −196 °C, obtained using a Micromeritics ASAP 2020 gas adsorption device. Before the measurement, the sample was degassed at 250 °C for 2 h. The catalyst reducibility was studied via temperature programmed reduction (TPR) analysis performed using a Micromeritics AutoChem 2920 equipment with a TCD detector. The analysis was carried out in the range 50–400 °C with a heating rate of 10 °C·min^{-1}, feeding 50 mL·min^{-1} of a 10% H_2/Ar mixture. Prior to the TPR analysis, the sample was outgassed under inert conditions as for the N_2 physisorption. The copper surface area (S_{Cu}), dispersion (D_{Cu}) and average surface-volume diameter (d_{Cu}^{SV}) were determined via N_2O oxidation followed by H_2 titration method developed by Van der Grift [68]. The analysis was carried out in the same equipment used for the TPR and consists in performing a first TPR measurement, whose hydrogen consumption is indicated by *X*. Thereafter, the temperature was reduced to 90 °C and the sample was outgassed under Ar flow for 2 h. The surface copper was oxidized feeding 50 mL·min^{-1} of a 2% N_2O/Ar mixture for 1 h. A second TPR analysis was carried out, whose hydrogen consumption (*Y*), is indicative of the number of Cu atoms dispersed on the surface of the catalyst. The copper surface area, dispersion and diameter were calculated with Eq. 26, Eq. 27 and Eq. 28, respectively, considering a Cu/N_2O = 2 titration stoichiometry and a surface atomic density of $1.4{\cdot}10^{19}$ $Cu_{at}{\cdot}m^{-2}$.

$$S_{Cu} = \frac{2Y{\cdot}N_{av}}{X{\cdot}M_{Cu}{\cdot}1.410^{19}} \tag{26}$$

$$D_{Cu} = \frac{2Y}{X}100\% \tag{27}$$

$$d_{Cu}^{SV} = \frac{6}{S_{Cu}{\cdot}\rho_{Cu}} \tag{28}$$

where N_{av}, M_{Cu} and ρ_{Cu} are the Avogadro's number, the copper molecular weight and density, respectively. X-ray diffraction (XRD) analysis in the 2θ range 10-120° was performed on the reduced catalyst with a MiniFlex600 machine (*Rigaku*) operating with a Ni β-filtered Cu-Kα radiant at 40 kV and 30 mA and a scan step of 0.05°/min. The diffraction peaks were identified according to the JCPDS database of reference compounds. The average diameter of the Cu-crystals was estimated via the Scherrer's equation (Eq. 29).

$$d_{Cu} = \frac{b\lambda}{FWHM\cos(\theta)} \tag{29}$$

where d_{Cu} is the dimension of the crystallites as if they were cubes, monodisperse in size, λ is the wavelength, *FWMH* is the width of the peak, 2θ is the scattering angle and b is a constant usually varying between 0.89 and 0.94. XPS measurements were performed both on the calcined and reduced catalyst, using a Kratos AXIS Ultra spectrometer, equipped with a monochromatic X-ray source, and a delay-line detector (DLD). Spectra were obtained using an aluminum anode (Al Kα = 1486.6 eV) operating at 150 W. The binding energies were internally calibrated setting the C1s peak position at 285 eV. The catalyst real density (ρ_{cat}) was measured using an automatic gas pycnometer instrument (Ultrapyc 1200e). The apparent density of the catalyst ($\rho_{b,cat}$) was calculated via the catalyst porosity (ε_{cat}), determined from the N_2 physisorption analysis. The catalytic tests were carried out in a stainless-steel reactor (d_{int}, 10 mm), loaded with 0.25 g of catalyst, diluted with 0.75 g of SiC, to ensure isothermal operation and prevent sintering phenomena. The catalyst and the SiC used for dilution were introduced in the reactor with the same particle size of 50–125 μm. Larger SiC particles were used as pre-heating bed, separated from the catalytic bed with c.a. 1 cm^3 of quartz-wool. The reactor was placed in an electric oven and heated more precisely via a heating mantle. The temperature was measured with two thermocouples, one at the beginning of the catalytic bed and one placed at the exit of the gases. Prior to the reaction tests, the catalyst was reduced *in situ* at 250 °C, with 50 mL·min^{-1} of a 50% H_2/N_2 mixture for 4 h. The reaction mixture was analysed with a compact gas chromatograph (Global Analyzer Solution ^{TM}, G.A.S.) equipped with a TCD detector and two packed columns (HayeSep Q 60–80 mesh and 5A molecular sieve) for the analysis of permanent gases (i.e., H_2, CO_2, CO and N_2) and an FID detector with capillary columns (Rtx-1, MTX-1 and MTX-QBond) for the analysis of the hydrocarbons. The experimental setup is sketched in Fig. 1. The reaction tests were performed in a range of temperature and pressure of 200–260 °C and

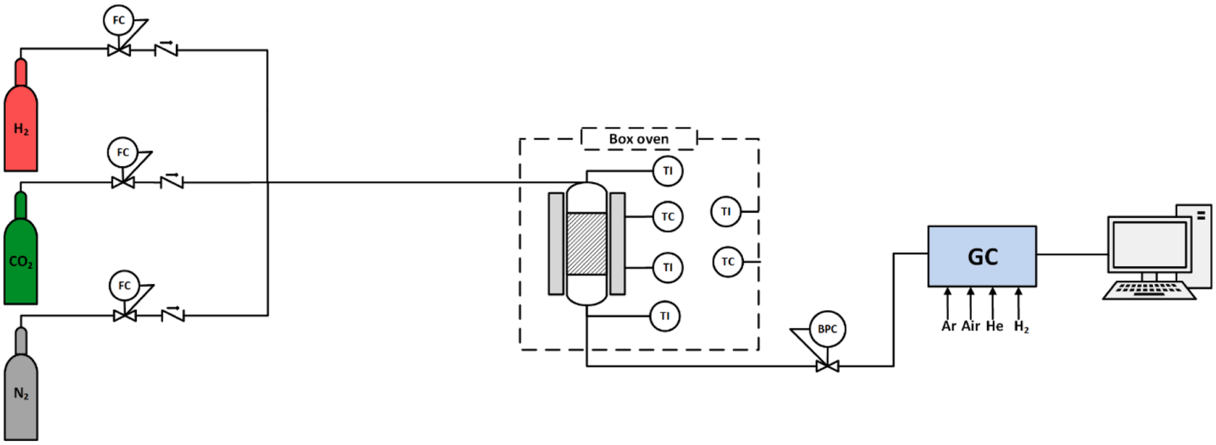

Fig. 1. Schematic representation of the experimental setup used for the catalytic tests. Gases (H_2, CO_2 and N_2) are fed from bottles (Linde). FC indicates mass flow controllers, TI and TC represent thermocouples and controllers, respectively. Pressure is controlled via a back pressure control system.

10–40 bar, respectively, feeding $H_2/CO_2/N_2$ mixtures in different proportion, to have a H_2:CO_2 molar ratio from 3 to 7, and a GHSV ranging from 7500 to 24000 $NL\cdot kg_{cat}^{-1}\cdot h^{-1}$. The carbon balance in the reaction was respected with a maximum error of 3%. The catalyst stability was observed within a long-term (100 h) test performed at 250 °C, 30 bar, H_2:CO_2 molar ratio of 3 and a GHSV of 9600 $NL\cdot kg_{cat}^{-1}\cdot h^{-1}$. The CO_2 conversion (X_{CO_2}), product yield (Y_i), product space time yield (STY_i) and product selectivity (S_i) were calculated according to Eq. 30–33, where i is either methanol or CO and w_{cat} is the catalyst weight. Methanol and CO where detected as the sole carbon species in the product mixture.

$$X_{CO_2} = \frac{F_{CO_2}^{in} - F_{CO_2}^{out}}{F_{CO_2}^{in}} \tag{30}$$

$$Y_i = \frac{F_i^{out}}{F_{CO_2}^{in}} \tag{31}$$

$$STY_i = \frac{F_i^{out}}{w_{cat}} \tag{32}$$

$$S_i = Y_i \cdot X_{CO_2} \tag{33}$$

A commercial $Cu/ZnO/Al_2O_3$ catalyst from Johnson Matthey (i.e. Katalko-51) was tested in the exact same conditions, to compare the novel catalyst with the benchmark technology.

4. Modeling

4.1. Fitting procedure and model discrimination

The fitting procedure was carried out entirely in MATLAB R2019a. The kinetic parameters were determined via the *fminsearch* optimization procedure, based on the Nelder-Mead simplex algorithm [69], which minimizes an error objective function (OF) that we defined as the sum of the root mean square errors (RMSE) between the experimental and calculated molar fraction of the carbon containing species (i.e., CO_2, CO and methanol) as follows:

$$RMSE_i = \sqrt{\frac{\sum_{k=1}^{N_{data}} \left(y_{i,k}^{calc} - y_{i,k}^{exp}\right)^2}{N_{data}}} \tag{34}$$

$$OF = RMSE_{CO_2} + RMSE_{CO} + RMSE_{MeOH} \tag{35}$$

Where N_{data} is the number of experimental data used for the kinetic fitting and y_i^{exp} and y_i^{calc} are the molar fractions of the component i at the exit of the catalytic bed determined experimentally and via the model prediction, respectively. The experimental data were imported in terms of y_i^{exp}, together with the corresponding boundary conditions, such as inlet flow (ϕ_o), inlet composition (y_i^0), temperature (T) and total pressure (P). On the other hand, the y_i^{calc} were determined, within the algorithm iterations, via the integral analysis method, thus solving the ODEs describing the mole balance equations in a fixed bed reactor (Eq. 36).

$$\frac{dF_i}{dw_{cat}} = \sum_{j=1}^{N_r} \left(r_j \nu_{ji}\right) \tag{36}$$

where F_i is the molar flow rate of the component i, w_{cat} is the catalyst weight, N_r is the total number of the reactions involved, ν_{ji} is the stoichiometric number of the component i in the reaction j, and r_j is the corresponding reaction rate expression, which is unknown. The mole balance equations were solved under the hypothesis of steady state regime, isothermal operation, negligible pressure drop along the catalytic bed and absence of internal diffusion and external mass transfer limitation. The first three hypothesis were confirmed experimentally: 1) the reaction performance was evaluated at steady state (i.e., when no changes in the outlet composition were recorder over time); 2) the temperature difference between the gas inlet and outlet positions was less than 1 °C and 3) the pressure difference between the gas inlet and outlet positions was less than 0.2 bar. The absence of mass transfer limitations was explored with preliminary experiments (details in S.I.) and was later confirmed with the Mear's [70] and Weisz-Prater [71] testing criteria.

The reaction rates (r_j) are function of the partial pressure of the components, and parameters such as kinetic (k_j), adsorption (b_i) and equilibrium constants (K_j^{eq}). The equilibrium constants (Table 3) were retrieved from literature [72].

The kinetic constant of each reaction (k_j) and adsorption constants of the components (b_i) are the parameter to be optimized throughout the algorithm. The kinetic constants were described as a function of a pre-exponential factor and an activation energy, following the Arrhenius'

Table 3
Equilibrium constant of all the reactions as a function of temperature [72].

Equilibrium constant	Expression	Units
K_1^{eq}	$\log_{10}K_1 = \frac{3066}{T} - 10.592$	bar^{-2} with T in K
K_2^{eq}	$\log_{10}K_2 = -\frac{2073}{T} + 2.029$	dimensionless with T in K
K_3^{eq}	$\log_{10}K_3 = \frac{5139}{T} - 12.6291$	bar^{-2} with T in K

law (Eq. 37) [73]. The adsorption constants, instead, were expressed as a function of the standard entropy ($\Delta S^0_{ads,i}$) and enthalpy of adsorption ($\Delta H^0_{ads,i}$), according to the van 't Hoff equation (Eq. 38). However, in some of the kinetic models considered in this study, the dependency on temperature of the adsorption constants is neglected (i.e., $\Delta H^0_{ads,i} \approx RT$) [5666]. Furthermore, to reduce the number of fitting parameters, some authors lumped the adsorption constants of some components together.

$$k_j = k_{j,0}\exp\left(-\frac{E_{a,j}}{RT}\right) \tag{37}$$

$$b_i = \exp\left(\frac{\Delta S^0_{ads,i}}{R}\right)\cdot\exp\left(-\frac{\Delta H^0_{ads,i}}{RT}\right) \tag{38}$$

The selected algorithm (*fminsearch*) requires an initial guess for the fitting parameters. Kinetic constant found in literature for the Cu-Zn-Al catalyst were implemented as initial guess, assuming these are likely of similar order of magnitude that the corresponding for our Cu-Ce-Zr catalyst [5513]. This minimizes the strong dependence that the algorithm has on the initial guess itself, and therefore increases the probability of obtaining meaningful results. To increase robustness of the model results, we setup a routine that evaluated the sensitivity of the model to the initial guess. This procedure consists of running the optimization algorithm in a loop, with newly obtained results as the initial guess. Thus, the convergence was reached when the difference between the algorithm output and the initial guess was less than 1%. Once the parameters of the best fit were obtained, the covariance matrix was computed with a second algorithm based on Levenberg-Marquardt method (*lsqnonlin*). From the covariance matrix, the standard deviation and the 95% confidence intervals, first indicators of the quality of the fit, were determined using the *nlparci* function in MATLAB. However, model discrimination techniques were necessary to find the set of rate expressions that best describe our system and, therefore, to gain insight into the reaction mechanism. A model was discarded at first when the physicochemical constraints (Table 4) were not respected. Thereafter, the significance of the model was assessed via the comparison of the variance of the lack of fit (s_1^2) and the experimental error (s_2^2), where $s_1^2 > s_2^2$. The *F*-test (Eq.40) was carried out in combination with the analysis of the *p*-value (Eq. 41) (i.e., probability that the data belong to the non-critical area of the Fisher distribution), assuming 95% level of confidence (i.e., $\alpha = 0.05$). The $F_{statistic}$ was first calculated according to Eq. 39, where s_1^2 is the variance of the lack of fit and s_2^2 is the variance of the experimental error. The $F_{critical}$ was retrieved from the Fisher distribution tables, considering N_{var} and $(N_{data} - N_{var})$ as degree of freedom, where N_{var} is the number of variables (parameters). The $F_{statistic}$ was then compared to the $F_{critical}$ (*F*-test, Eq.40).

$$F_{statistic} = \frac{s_1^2}{s_2^2} \tag{39}$$

$$F_{statistic} < F_{critical} = F_{(1-\alpha)}(N_{var}; N_{data} - N_{var}) \tag{40}$$

$$p > \alpha \tag{41}$$

As a result, the kinetic models fulfilling the physicochemical constraints were evaluated according to: 1) the value of the objective function, 2) the parity plots of the experimental and calculated flow rates of the carbon species, and 3) the outcome of the *F*-test and *p*-value.

Table 4
Physicochemical constraints of the kinetic parameters.

Parameter	Physicochemical constraint
Pre-exponential factor, $k_{j,0}$	$k_{j,0} > 0$
Activation energy, $E_{a,j}$	$E_{a,j} > 0$
Enthalpy of adsorption, $\Delta H^0_{ads,i}$	$\Delta H^0_{ads,i} < 0$
Entropy of adsorption, $\Delta S^0_{ads,i}$	$0 < -\Delta S^0_{ads,i} < S^0_{g,i}$

4.2. Testing criteria for mass transfer limitation

The absence of mass transfer (MT) limitations was evaluated according to the criteria reported in Table 5, where the Carberry (*Ca*) and the second Damkohler number (Da_{II}) are defined per component. The order of reaction with respect to the component *i* (n_i) was estimated with Eq. 42, where r_i^+ is its forward reaction rate [74]. Such derivation is specifically defined for complex reaction rates equation such as a LHHW kinetic. The correlations used for the mass transfer coefficient (k_{gs}) and the effective diffusivity (D_e) are reported in SI.

$$n_i = p_i\frac{\partial}{\partial p_i}\ln(r_i^+) \tag{42}$$

5. Results

5.1. Catalyst properties and reaction performance

Table 6 summarizes the main physical properties of the Cu/CeO$_2$/ZrO$_2$ catalyst. The textural properties of the catalyst are in line with the literature [49,50]. The N$_2$ physisorption analysis revealed an isotherm of type IV with hysteresis (**Figure S1**), which is typical of a mesoporous material (i.e., pores in the range of 2–50 nm). The TPR profile (**Figure S4a**) exhibits two peaks at 204 °C and 231 °C, after deconvolution. No further reduction of the support, due to H$_2$ spillover, was measured. As a result, a reduction temperature of 250 °C is believed to be sufficient to reduce all the CuO, prior to the reaction tests. The XRD spectra on the calcined and reduced catalyst (**Figure S2**) show the typical diffraction peaks of CuO at 2θ of 35.5° and 38.7° and of Cu at 2θ of 43.3° and 50.4°, respectively. The disappearance of the CuO peak in the XRD spectrum of the reduced sample (**Figure S2b**) does not necessarily indicate the presence of sole metallic Cu, as CuO crystals smaller than 3–5 nm cannot be detected, as well as the Cu that is in contact with the Ce-Zr phases via O-bridges. The more complex Ce-Zr oxide phase was analyzed via XPS (**Figure S3**). We confirmed the presence of the Ce^{3+} valence, which is introduced by the zirconia phase, as reported elsewhere [49,50]. The CuCeZr catalyst of this study is characterized by a Ce^{4+}/Ce^{3+} ratio of c.a. 3.53, which was calculated through the integration of the corresponding peaks of the XPS spectra. A detailed discussion on the XPS results is given in S.I. The catalyst composition according to the MP-AES method is 52 wt% of CuO, 22 wt% of CeO$_2$ and 26 wt% of ZrO$_2$. This composition is very close to the theorical value, indication of the reliability of the synthesis method. In Fig. 2**a** the catalyst performance during CO$_2$ hydrogenation is compared to that of the benchmark formulation (i.e., the CuZnAl from JM). The CuCeZr catalyst shows a much higher methanol production compared to CO, with a crossover temperature (i.e., T_{cross} temperature beyond which $\mathrm{STY_{CO}} > \mathrm{STY_{MeOH}}$) of ca. 240 °C. On the contrary, the benchmark catalyst shows a $\mathrm{STY_{CO}}$ larger than $\mathrm{STY_{MeOH}}$ over the entire temperature range. Since our catalyst formulation and preparation methods is a reproduction of previous works [49,50], we also compare the performance of this catalyst with that of the original reports by Shi et al., [49] (Fig. 2**b**). The catalyst synthesized in this work shows higher methanol yield with respect to the different formulations proposed by Shi et al., However, the physicochemical properties of our CuCeZr are further

Table 5
Testing criteria for the exclusion of internal (intraparticle) and external (gas–solid) mass transfer limitation.

Criteria	Formula-test	Type of MT excluded
Mear's [70]	$Ca = \frac{r_{i,obs,V}\cdot d_p/2\cdot n_i}{k_{gs}C_{ib}} \leq 0.15$	External mass transfer
Weisz-Prater [71]	$Da_{II} = \frac{r_{i,obs,V}\cdot(d_p/2)^2\cdot n_i}{D_e C_{is}} \leq 0.3$	Internal diffusion

Table 6
Physical properties of the $Cu/CeO_2/ZrO_2$ catalyst.

Property	Value
BET surface area, S_{BET} $(m^2 \cdot g^{-1})$	79
Pore volume, $P.V.$ $(cm^3 \cdot g^{-1})$	0.26
Pore diameter, $P.D.$ (nm)	9.5
Average Cu diameter, d_{Cu} (nm)*	10.4
Surface-to-volume Cu diameter, d_{Cu}^{SV} (nm)	11.6
Cu dispersion, D_{Cu} (%)	8.56
Cu specific surface area, S_{Cu} $(m^2_{Cu} \cdot g^{-1})$	58
Catalyst solid density, ρ_{cat} $(g \cdot cm^{-3})$	7.53
Catalyst porosity, ε_{cat} $(m^3_{pore} \cdot m^{-3}_{cat})$	0.66
Catalyst apparent density, $\rho_{b,cat}$ $(g \cdot cm^{-3})$ **	2.56

* Determined via XRD; **Include the solid porosity.

improved with the calcination temperature (i.e., 450 °C), according to the optimization reported by Wang et al., [50]. Unfortunately, insufficient details on the results reported by Wang et al., made a direct comparison with our results unreliable. However, assuming a catalyst density of 2.56 $g \cdot cm^{-3}$ (i.e., value we measured), the STY_{MeOH} they obtained at the same conditions is c.a. 6.6 $mmol \cdot h^{-1} \cdot g^{-1}_{cat}$, which compares with the value reported in Fig. 2**b**. The agreement of our results with literature underline the credibility of the method. Furthermore, they emphasize the promising performance of the CuCeZr catalyst with respect to the benchmark technology, in view of the CO_2 valorization to methanol.

5.2. *Model discrimination and proposed reaction mechanism*

Table 7 reports the information required for the model discrimination procedure, as discussed in Section 4.1. The rate determining step analysis (RDS) is carried out only when the author(s) reported the details behind the model derivations (i.e., Graaf and Slotboom). The discrimination between the different options proposed by Graaf and Slotboom is reported in S.I. and is based on the same criteria shown here. Both the models developed by Park and Seidel did not fulfil all the physicochemical constraints, thus, the statistics analysis was not carried out. It is worth noticing that all the models which do not consider the formation of methanol from CO (reaction 3), resulted in a low *p-MeOH* (i.e., *p*-value for methanol) which indicates the tendency of the model towards a scarce prediction of the methanol outlet molar fraction. This result anticipates the importance of considering the contribution of both CO and CO_2 to the methanol synthesis, especially when CO_2 is the sole carbon source.

The model with the lowest RMSE (which corresponds to the final value of the objective function) and the largest *p*-values for the carbon species is the one proposed by Graaf. As a result, we select this model (Graaf-$A_3B_1C_3$, where $A_3B_1C_3$ refer to the specific combination of RDS) to be the most representative of our system. The kinetic parameters obtained from the fitting procedure are provided in Table 8. The accuracy of the parameter estimation is represented by the parity plots of CO_2, CO, H_2 and methanol (Fig. 3). The orders of magnitude of all the parameters are in line with the literature, especially when compared to the values retrieved from Graaf et al. Nevertheless, given the differences in the reaction rate expressions (i.e., $A_3B_1C_3$ for our CuCeZr catalyst versus the $A_3B_2C_3$ for the CuZnAl reported by Graaf), the comparison between the two kinetic models – and catalyst – is fair when observed in terms of reaction rates, rather than kinetic constants. Such analysis is addressed in Section 5.5. On the other hand, the adsorption term corresponding to the first and second active sites (i.e., Θ_1 and Θ_2, respectively) do not differ from the original model. Therefore, in Table 9 we compare the values of our adsorption constants to the same constants

Table 7
Comparison of the kinetic models reparametrized for the CuCeZr catalyst.

Property	BF [59]	Graaf [58]	Henkel [54]	Park [65]	Seidel [56]	Slotboom [66]
RDS*	–	$A_3B_1C_3$	–	–	–	4 –11
P-C Const.**	✓	✓	✓	×	×	✓
RMSE · 10^2	1.684	1.512	1.541	–	–	1.650
$F_{statistic}$	0.5419	0.2450	0.2871	–	–	0.4344
$F_{critical}$	1.993	1.917	1.993	–	–	2.254
p-CO$_2$	0.9761	0.9035	0.8919	–	–	0.9826
p-CO	0.5157	0.9601	0.9453	–	–	0.4903
p-MeOH	0.4695	0.9552	0.3138	–	–	0.1490

* The result of the Rate-Determining-Step (RDS) analysis is reported for the models which provided such tool, as described in section 3.

** Physicochemical constraints: if not fulfilled, statistics analysis is not carried out.

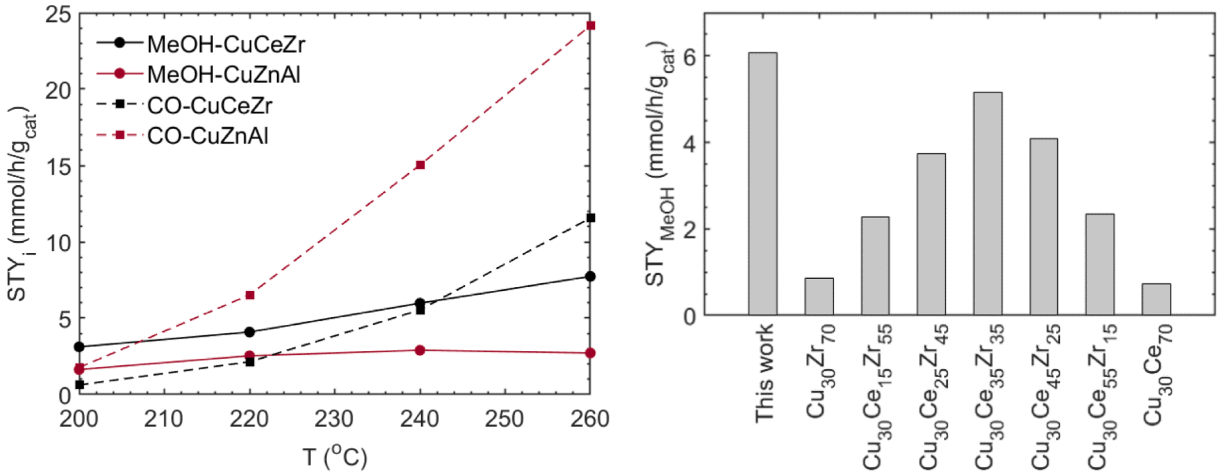

(a) (b)

Fig. 2. Methanol (MeOH) and CO space time yield (STY) as a function of temperature for the CuCeZr and the benchmark CuZnAl catalyst (a) and comparison of the methanol space time yield (STY_{MeOH}) at 250 °C with the performance of $CuCe_xZr_yO$ retrieved from literature [49] (b). Other experimental conditions: total pressure of 30 bar, H_2:CO_2 molar ratio of 3.

Table 8

Kinetic parameters for the Graaf model ($A_3B_1C_3$). The adsorption constants b_i need to be calculated according to Eq. 13, considering $b_{i,0} = \exp\left(\Delta S^0_{ads,i}/R\right)$.

Kinetic parameter	Value	Units
k_{10}	$(7.103 \pm 0.351)\cdot 10^{-1}$	$mol\cdot kg_{cat}^{-1}\cdot s^{-1}\cdot bar^{-2.5}$
k_{20}	$(2.765 \pm 0.118)\cdot 10^{11}$	$mol\cdot kg_{cat}^{-1}\cdot s^{-1}\cdot bar^{-1.5}$
k_{30}	$(1.416 \pm 0.097)\cdot 10^{9}$	$mol\cdot kg_{cat}^{-1}\cdot s^{-1}\cdot bar^{-2.5}$
E_{a1}	$(3.378 \pm 0.224)\cdot 10^{4}$	$J\cdot mol^{-1}$
E_{a2}	$(1.342 \pm 0.089)\cdot 10^{5}$	$J\cdot mol^{-1}$
E_{a3}	$(1.204 \pm 0.094)\cdot 10^{5}$	$J\cdot mol^{-1}$
$b_{CO_2,0}$	$(6.173 \pm 0.327)\cdot 10^{-7}$	bar^{-1}
$\Delta H^0_{ads,CO_2}$	$-(5.668 \pm 0.451)\cdot 10^{4}$	$J\cdot mol^{-1}$
$b_{CO,0}$	$(3.561 \pm 0.296)\cdot 10^{-3}$	bar^{-1}
$\Delta H^0_{ads,CO}$	$-(8.438 \pm 0.364)\cdot 10^{3}$	$J\cdot mol^{-1}$
$b_{H_2O,H_2\,0}$ *	$(3.521 \pm 0.511)\cdot 10^{-12}$	$bar^{-0.5}$
$\Delta H^0_{ads,H_2O,H_2}$ *	$-(1.242 \pm 0.105)\cdot 10^{5}$	$J\cdot mol^{-1}$

* Parameters to determine the combined adsorption constant of H_2O and H_2 ($b_{H_2O}/\sqrt{b_{H_2}}$).

calculated by Graaf at 200 and 260 °C. From the reaction rate expressions (Eq. 6–10), we see that the adsorption constants of CO_2 and CO contribute also to the driving force (i.e., numerator of the reaction rate). As a result, the prediction of their effect on the reaction rate is not straightforward. On the contrary, the combined adsorption of H_2O and H_2 (i.e., $b_{H_2O}/\sqrt{b_{H_2}}$) contributes only to the adsorption term in the denominator, hindering the reaction rate. Since our constant is order of magnitude higher than the one derived by Graaf, this leads to the conclusion that our catalyst is either more sensitive to water or to H_2 adsorption.

The model discrimination allows us not only to identify a model which better predicts the performance of our catalyst, but, most importantly, to gain some insights into the reaction mechanism itself. According to the assumptions behind the model developed by Graaf

Table 9

Comparison of the values of the adsorption constants obtained in this work and by Graaf at 200 and 260 °C.

Adsorption constant	This work (200–260 °C)	Graaf (200–260 °C)
b_{CO_2}, bar^{-1}	1.117 –0.2207	4.571 –0.7823
b_{CO}, bar^{-1}	$(3.042 - 2.389)\cdot 10^{-2}$	3.171 –0.8313
$b_{H_2O}/\sqrt{b_{H_2}}$, $bar^{-0.5}$	181.4 –5.19	$(5.389 - 4.238)\cdot 10^{-8}$

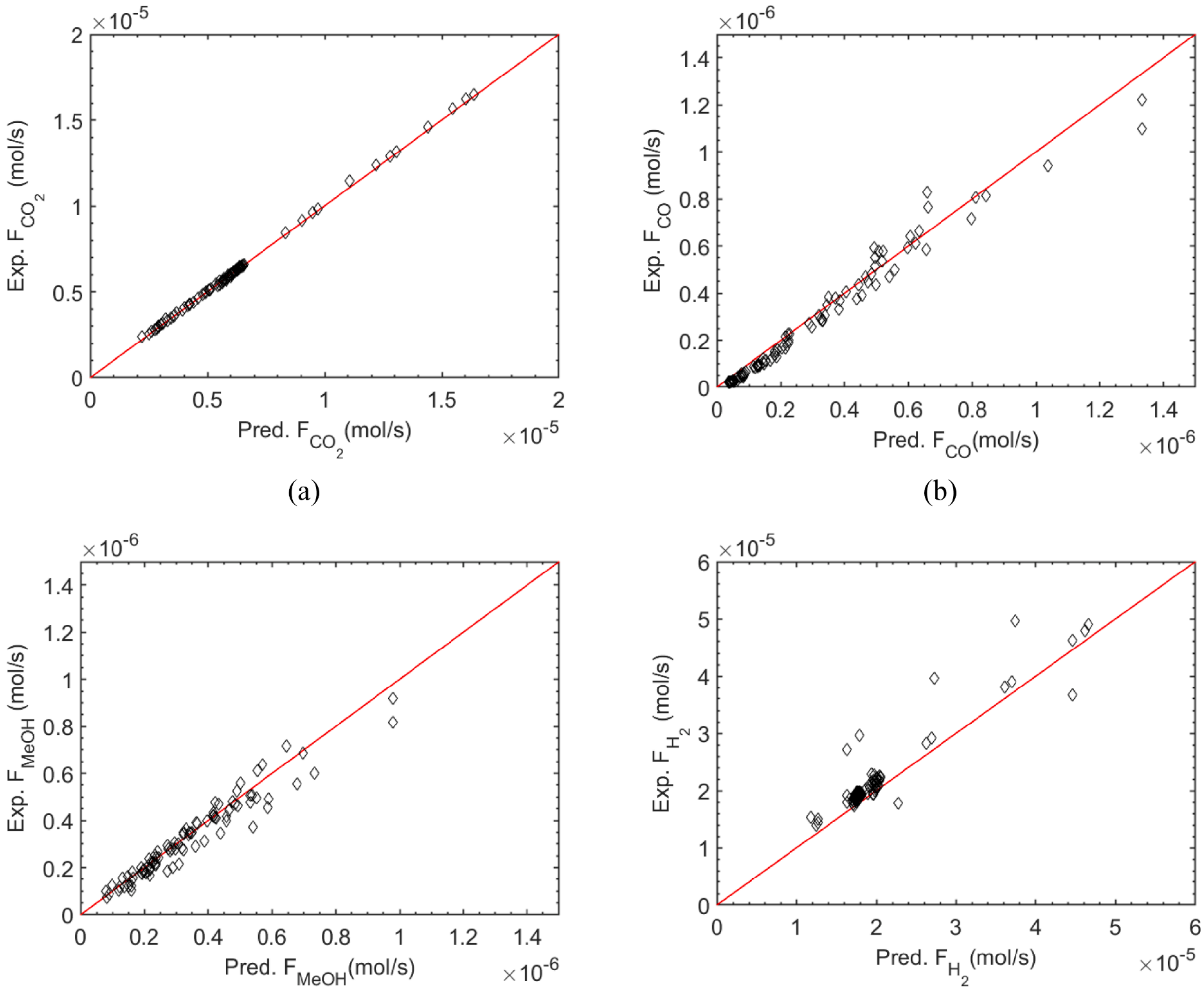

(a) (b) (c) (d)

Fig. 3. Parity plot representing the accuracy of the parameter estimation for the outlet flow rate of CO_2 (a), CO (b), Methanol (c) and H_2 (d). The corresponding experimental data points are reported in S.I.

et al., we can distinguish between two active centers in the structure of the CuCeZr catalyst, which is in agreement with what was hypothesized in literature [49]: 1) the metallic copper (i.e., Cu^0), where the dissociative adsorption of H_2 occurs and 2) the oxygen defects within the Ce/Zr interface, where the CO_2 molecule adsorbs and activates. The H species spillover towards the carbon atom of the activated CO_2 to begin a series hydrogenation steps, knowns as “formate” route. The reaction pathway is sketched in Fig. 4. According to the formate path, methanol can be either synthesized directly from CO_2 (direct route) or indirectly from the CO produced via the rWGS reaction. The two routes overlaps when the H_2CO intermediate forms, sharing the last two steps which then lead to the formation of methanol. However, at the point where the CO_{s1} (i.e., CO adsorbed) intermediates appears, an equilibrium between the adsorbed CO and the CO released to the gas phase explains a certain selectivity to CO. The relative contribution of CO and CO_2 to the methanol synthesis depends on different factors such as temperature, H_2 concentration and the distribution of the Cu^0 active sites with respect to the oxygen vacancies. Nevertheless, for a fixed catalyst composition, only reaction conditions can affect the fraction of methanol produced via the direct and indirect paths. A detailed discussion on this aspect is given in Section 5.5.

In Fig. 4, the limiting steps of the three reactions are also marked. In particular, the slowest steps are the formation of the H_3COO_{s1}, $HCOO_{s1}$ and H_3CO_{s1} intermediates for the reaction 1, 2 and 3, respectively. This result is in agreement with the *in situ* DRIFT studies carried out by Wang et al., [50], where the formation of the formate (i.e., $HCOO_{s1}$) through the first hydrogenation of the carbon atom is defined as “the slowest and key step”.

At this stage, being the reaction rate expressions determined, we could estimate the order of the reaction with respect to CO_2 (n_{CO_2}) and evaluate the Ca and Da_{II} numbers. We observed that in our experimental conditions, n_{CO_2} ranges between 0.094 and 0.62. Furthermore, both the external mass transfer and internal diffusion limitation resulted to be negligible, being the maximum value of Ca and Da_{II} of $1.4 \cdot 10^{-3}$ and $7.1 \cdot 10^{-5}$, respectively. This result confirms our earlier conclusion that the experiments were carried out under kinetic regime.

5.3. Analysis of the catalyst performance: Experiments vs model prediction

In this section, we discuss the catalyst performance as a function of the reaction conditions explored both experimentally and via model predictions. Experimental points and simulation results are combined in the same graphs, to show at the same time the quality of the fit. A detailed analysis of the thermodynamic equilibrium is reported in S.I.. Furthermore, to underline the compatibility of our results with the adopted equilibrium constant, the catalyst performance as a function of temperature and pressure – both experimental and modeling data – are reported together with the corresponding thermodynamic limit in **Figure S10.**

First, from Fig. 5 we observe that the kinetic model (solid lines) describes accurately the experimental reaction performance (points), in terms of X_{CO_2} (Fig. 5**a**), Y_{MeOH} (Fig. 5**b**) and Y_{CO} (Fig. 5**c**) as a function of the space velocity (GHSV) at various temperatures. As expected from a kinetically controlled system, the conversion decreases with the space velocity, being the contact time of the gases with the catalytic bed shorter. Furthermore, Y_{MeOH} and Y_{CO} show the same trend as X_{CO_2}, leading to the conclusion that the contact time does not affect the product distribution in the range we explored. As a result, when employing a GHSV in the range 7500–24000 $NL \cdot kg_{cat}^{-1} \cdot h^{-1}$, the CO contribution to the formation of methanol appears instantaneously, so that CO does not require additional contact time to react with the adsorbed hydrogen. Indeed, if that was the case, we would have observed an optimum in Y_{CO} as a function of GHSV. Additionally, X_{CO_2}, Y_{MeOH} and Y_{CO} all show a clear increase with temperature, resulting from the positive effect that temperature has on all the reaction rates. Finally, it is important to notice that at the lowest GHSV (**Figure S10**), the catalyst performance approach the thermodynamic equilibrium only at 260 °C (i.e., highest reaction rate), where the thermodynamic value of X_{CO_2}, Y_{MeOH} and Y_{CO} at 30 bar is 21.1 %, 8.04 % and 13.1 %, respectively. As a result, in the temperature region 200–260 °C X_{CO_2}, Y_{MeOH} and Y_{CO} still displays an exponential increase with temperature (i.e., kinetic regime).

Fig. 6 displays the effect of temperature and total pressure on the methanol (Y_{MeOH}) and CO yield (Y_{CO}). As anticipated from Fig. 5, temperature positively affects all the reactions, since the effect of kinetics (i.e., Arrhenius type) overcomes the thermodynamics. Besides, we observe that the effect of temperature on Y_{MeOH} (Fig. 6**a**) is more significant as total pressure increases (i.e., the increase in Y_{MeOH} from 200 to 260 °C is of 91% and 193% at 10 and 40 bar, respectively). On the contrary, Y_{CO} decreases with pressure and, at the same time, it keeps the same trend vs temperature, independently on the total pressure. As a result, the temperature of crossover shifts to higher values when pressure increases: at 10 bar the crossover occurs at c.a. 216 °C, while at 40 bar $Y_{MeOH} > Y_{CO}$ in the temperature region we explored (i.e., 200–260 °C).

In Fig. 6**b** the effect of total pressure in the range of 10–40 bar is underlined: Y_{CO} and Y_{MeOH} exhibit two opposite trends, and the effect becomes more significant at higher temperatures (i.e., faster increase/decrease vs pressure). As discussed in section 4.2, methanol is formed via two parallel routes: 1) the direct one, which involves only reaction 1 and 2) the indirect one, which involves reaction 2 and 3, in series. As a result, when feeding only CO_2 and H_2 or, more generally, with CO_2-rich streams, the direct route is faster than the indirect, since the latter needs the formation of CO first (i.e., r_3 is negligible for low values of p_{CO}). As soon as CO is formed, r_3 increases, causing an increase in methanol formation and, at the same time, a consumption of CO, which acts both

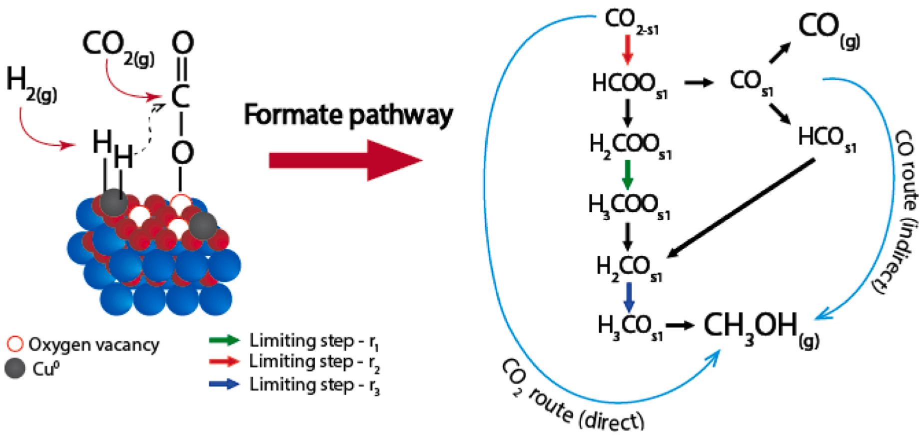

Fig. 4. Schematic representation of the reaction mechanism. On the left: dissociative adsorption of the H_2 molecule on metallic copper and oxygen adsorption of the CO_2 molecule onto the oxygen vacancies created by the CeZr oxide solution. The adsorbed H tends to interact with the carbon leading to the formate path. On the right: the formate path proceeds according to a series of hydrogenation steps, where methanol can be formed either via the direct route (i.e., directly from CO_2) or via the indirect one (i.e., via CO coming from the rWGS reaction).

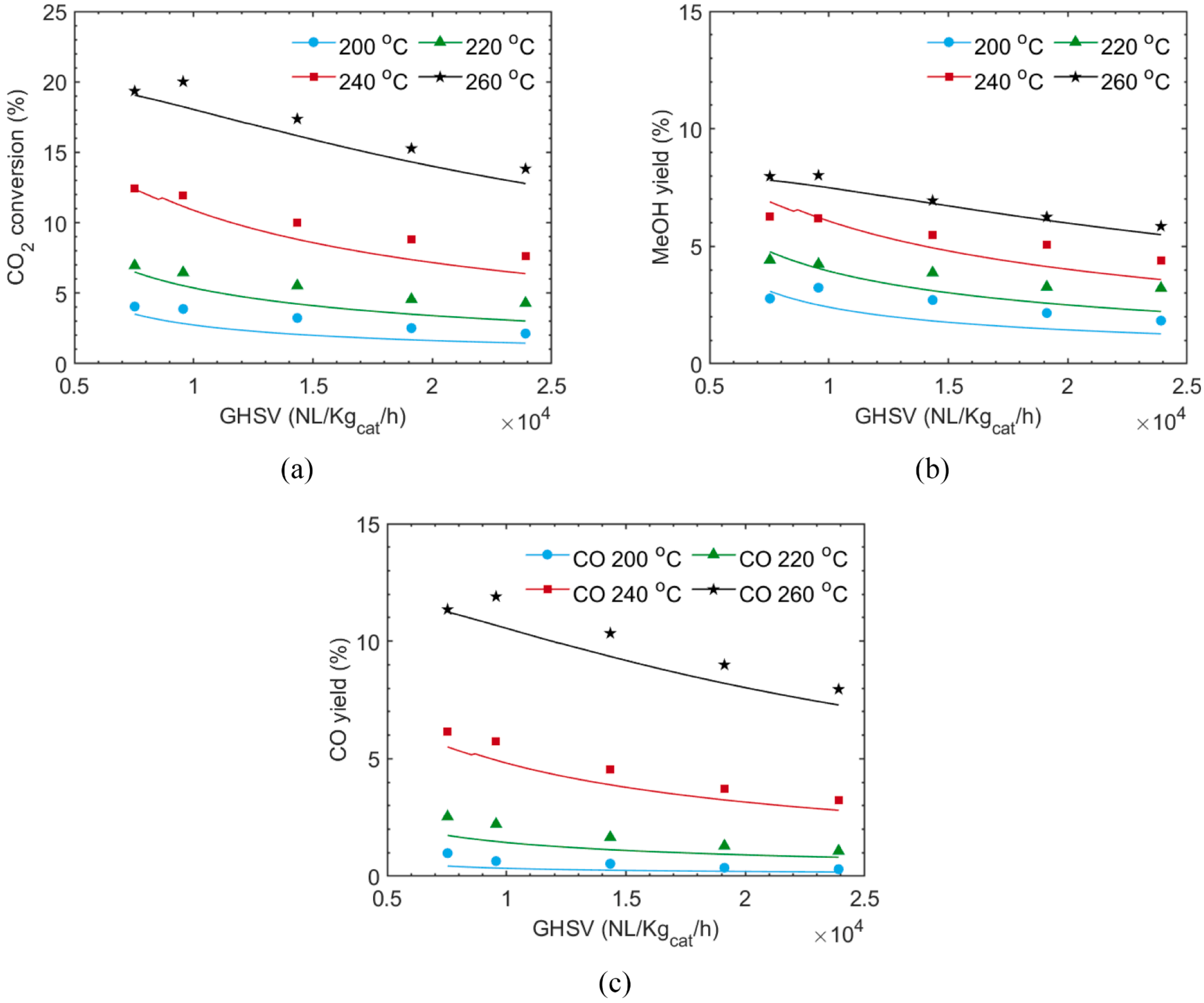

(a)

(b)

(c)

Fig. 5. CO_2 conversion (a) methanol yield (b) and CO yield (c) as a function of the GHSV at 200 °C (light blue), 220 °C (green), 240 °C (red) and 260 °C (black). Other experimental conditions: H_2:CO_2 molar ratio of 3, pressure of 30 bar. Markers and lines represent experimental points and simulation results, respectively.

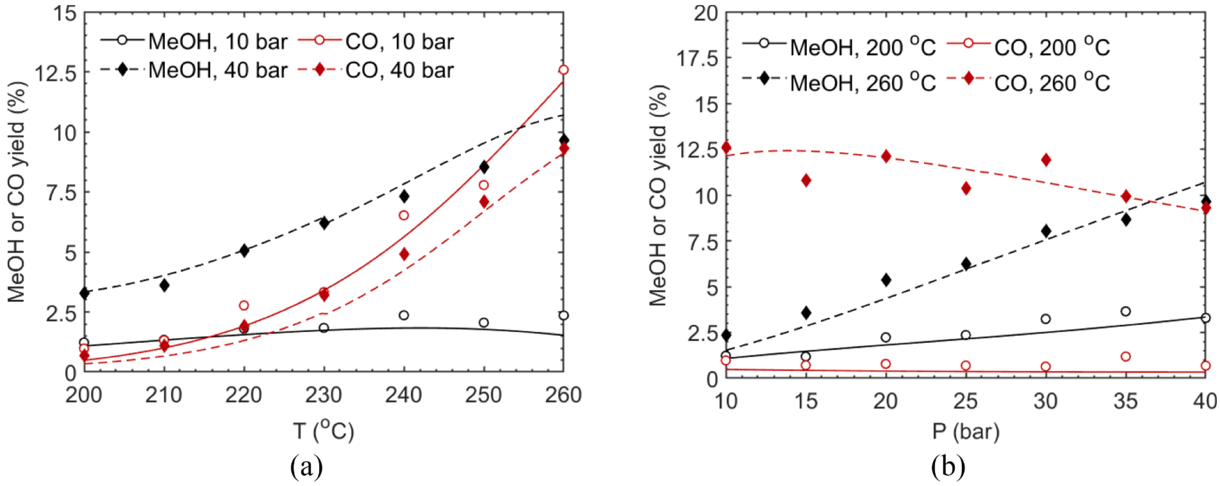

(a)

(b)

Fig. 6. Methanol (black) and CO (red) as a function of a) temperature at 10 (solid lines, empty markers) and 40 bar (dashed lines and filled markers) and b) pressure at 200 (solid lines, empty markers) and 260 °C (dashed lines and filled markers). Other experimental conditions: H_2:CO_2 molar ratio of 3, GHSV of 9600 $NL \cdot kg_{cat}^{-1} \cdot h^{-1}$. Markers and lines represent experimental points and simulation results, respectively.

as a product and a reactant. Such an effect is more noticeable at greater temperatures, because of faster reactions (i.e., the effect of pressure anticipates).

Besides the effect of total pressure, a higher H_2 concentration in the feed (i.e., higher molar feed ratio H_2:CO_2) causes an increase in both Y_{MeOH} and Y_{CO} (Fig. 7**a**), independently of temperature. However, Y_{MeOH}

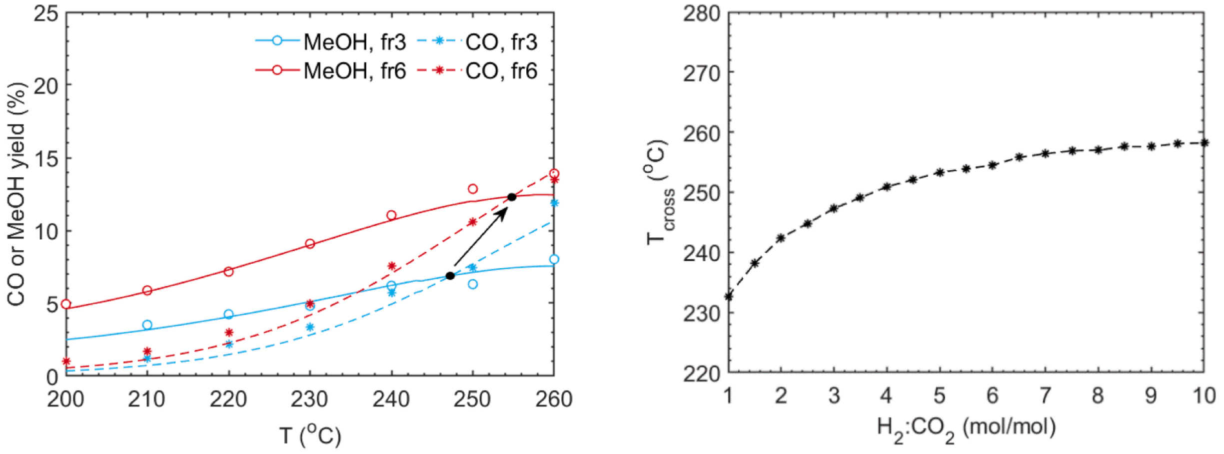

(a) (b)

Fig. 7. Methanol (solid lines with circles) and CO (dashed lines with stars) as a function of temperature at H_2:CO_2 = 3 (fr3, light blue lines) and H_2:CO_2 = 6 (fr6, red lines); markers and lines represent experimental points and simulation results, respectively (a). Temperature of crossover between methanol and CO yield (T_{cross}) as a function of the H_2:CO_2 molar ratio, as predicted by the kinetic model (b). Other experimental/modeling conditions: total pressure of 30 bar, GHSV of 9600 $NL \cdot kg_{cat}^{-1} \cdot h^{-1}$.

increases more than Y_{CO}, shifting again the crossover point towards higher temperatures. As shown in Fig. 7**a**, the model describes quite precisely the crossover point (T_{cross}). Therefore, we used the model to predict the reaction performance in a wider range of H_2:CO_2 (1–10). We found that T_{cross} monotonically increases up to an asymptotic value of 258 °C at around H_2:CO_2 of c.a. 7 (Fig. 7**b**). As a matter of fact, a higher H_2 concentration facilitates its adsorption on the active sites, increasing the surface concentration of H_{s2}. As a result, as soon as CO forms, its hydrogenation is faster than its desorption to the gas phase, which enhances the indirect pathway once again (i.e., higher Y_{MeOH}). However, when all the active sites for H_2 adsorption (i.e., Cu^0) are saturated with H_2, a further increase in its partial pressure does not affect the reaction rates anymore.

5.4. *Predictive capability of the kinetic model*

Once defined the reaction rates, we tested the predictive capability of the model by using the model to calculate both X_{CO_2} and Y_{MeOH} and comparing those values to an independent set of experiments (i.e., experimental data not used for the kinetic fitting). The kinetic model predicts quite accurately the experimental points obtained at lower GHSV (i.e., 2880 $NL \cdot kg_{cat}^{-1} \cdot h^{-1}$, last 4 points) and at lower pressure (i.e., 28 bar, first two points), with a maximum deviation of 2.1% and 2.2% for X_{CO_2} and Y_{MeOH}, respectively (Fig. 8).

5.5. *Analysis of the reaction rates: Role of CO and CO_2 hydrogenation*

In this section, we analyse in more details the reaction rates and the relative contribution of the CO_2 and CO hydrogenation (i.e., direct and indirect pathway, respectively) to the methanol formation. First, we calculate the reaction rates at different temperatures, via a theoretical differential analysis (i.e., assuming conversion values lower than 5%) at 30 bar and H_2:CO_2 ratio of 3 (Fig. 9**a**). We observe that r_1 is the highest reaction rate at temperatures below c.a. 240 °C. Therefore, at low temperatures, the CO_2 hydrogenation to methanol is the fastest reaction, being its activation energy the lowest (Table 8). However, r_1 is the only reaction rate showing an optimum in the temperature range we explored. It is clear indeed, that r_1 approaches the equilibrium as temperature increases, being its value very close to zero at 260 °C. As a result, we observe here the two opposite effects of kinetics and thermodynamics of an exothermic reaction. On the contrary, r_2 and r_3 are

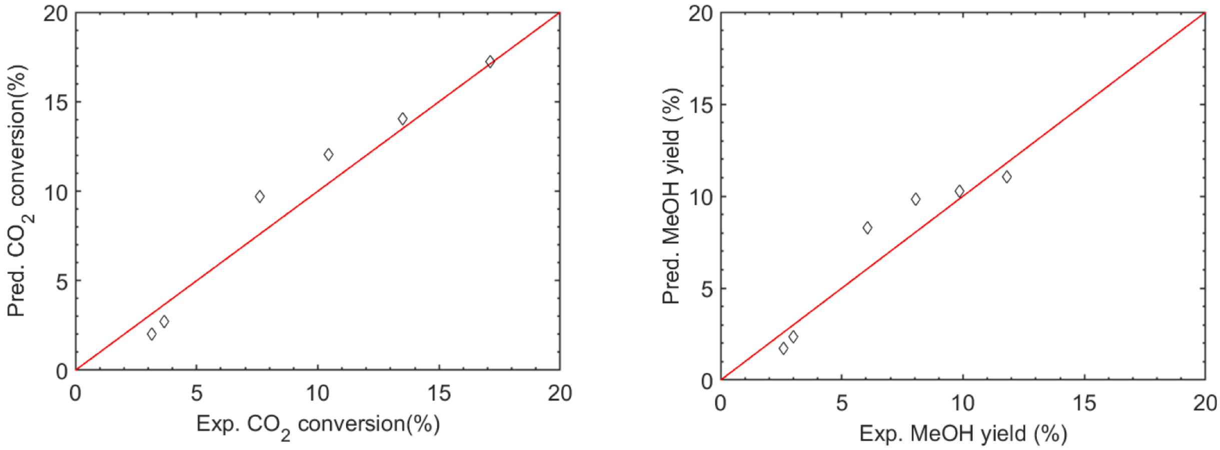

(a) (b)

Fig. 8. Parity plot representing the validation of the kinetic model, reporting the predicted X_{CO_2} vs the experimental X_{CO_2} (a) and the predicted Y_{MeOH} vs the experimental Y_{MeOH} (b). The corresponding experimental data are reported in S.I. (Table S1).

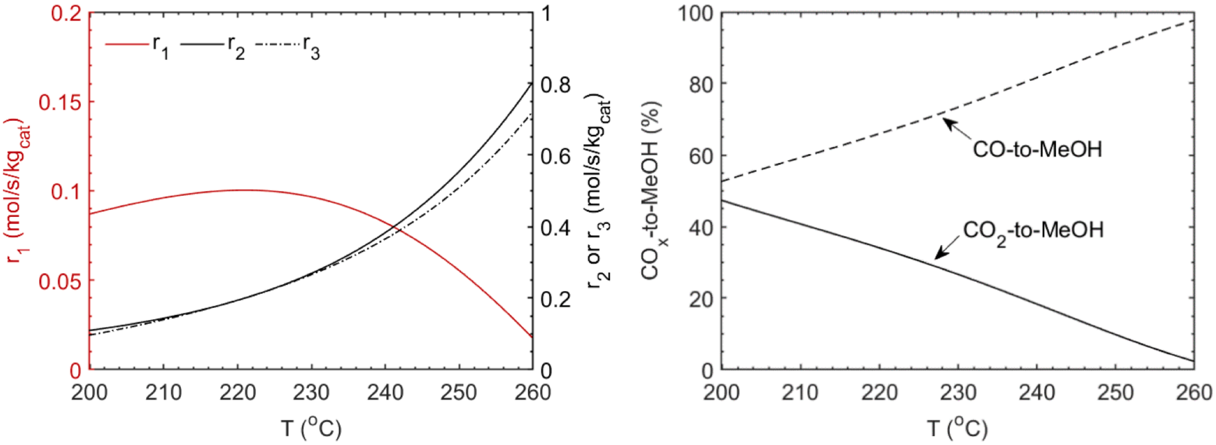

(a) (b)

Fig. 9. Reaction rates of the CuCeZr system as a function of temperature (a) and relative contribution of CO and CO_2 to the formation of methanol as a function of temperature on the CuCeZr catalyst (b). The results were obtained via simulations, at a pressure of 30 bar, a H_2:CO_2 ratio of 3 and a GHSV of $2.15\cdot10^5$ $NL\cdot kg_{cat}^{-1}\cdot h^{-1}$.

quite far from the equilibrium and both display the typical exponential behaviour of kinetically controlled reactions. In addition, reaction 2 and 3 proceed with similar velocities, with r_2 being slightly faster as temperature increases (i.e., $r_2/r_3 = 1.1$ at 260 °C). We clearly see that the two pathways for methanol formation behave differently with temperature. As a result, the relative contribution of CO_2 and CO to methanol synthesis changes as temperature increases (Fig. 9**b**). At 200 °C, CO and CO_2 contributes almost equally (i.e., 51.5% and 47.4% at 200 °C, respectively). As temperature increases, CO-to-MeOH and CO_2-to-MeOH exhibit opposite trends, with CO-to-MeOH reaching a value of c.a. 100% at 260 °C. This result reveals why methanol selectivity does not decay with temperature as fast as it does on the CuZnAl catalyst (Fig. 2**a**) and underlines the importance of designing a catalyst in such a way that CO adsorption is strong enough, to be able to proceed with the hydrogenation steps and form methanol, rather than desorb to the gas phase and contaminate the product stream.

In Fig. 10**a**, instead, we report the reaction rates as a function of the H_2:CO_2 ratio at 200 °C and 30 bar. All the reaction rates remarkably increase with the H_2 concentration. In particular, when H_2:CO_2 goes from 1 to 10, r_1, r_2 and r_3 increase by ca. 30, 17 and 60%, respectively. As a matter of fact, all the direct reactions exhibit a positive order with respect to H_2. However, expectedly, when the Cu^0 active sites are saturated with H_2, a further increase in the H_2 concentration corresponds to a dilution of the carbon species, such as CO_2 and CO, which also influence positively the reaction rates. This explains the slight decrease of the reaction rate (more noticeable for r_2 and r_3) beyond H_2:CO_2 of c.a. 7, which is in agreement with the result reported in Fig. 7**b**. For completion, in Fig. 10**b** we also report the relative contribution of CO_2-to-MeOH and CO-to-MeOH crosses at H_2:CO_2 of c.a. 1.5, with CO showing the predominant contribution beyond the crossing point. This is a clear consequence of the influence that the H_2:CO_2 ratio has on the reaction rate. For H_2:CO_2 larger than 1.5, $r_3 > r_1$ and the contribution of CO surpasses that of CO_2, following a trend which corresponds to the reaction rates r_3 and r_1, respectively.

To underline the potential of the CuCeZr catalyst, we propose here a comparison with the benchmark formulation (i.e., CuZnAl) in terms of reaction rates. First, the model derived by Graaf et al., was implemented and validated with the experimental results obtained for the CuZnAl catalyst (details on the validation are given in S.I.). Therefore, the kinetic model we adopted for such comparison is representative of the CuZnAl system and can be used for predictive studies. As depicted in Fig. 11**a**, the CO_2 consumption rate ($-r_{CO_2}$) increases exponentially with temperature and it is quite similar for both catalysts, with the CuCeZr showing a slightly faster consumption. However, the CuCeZr catalyst

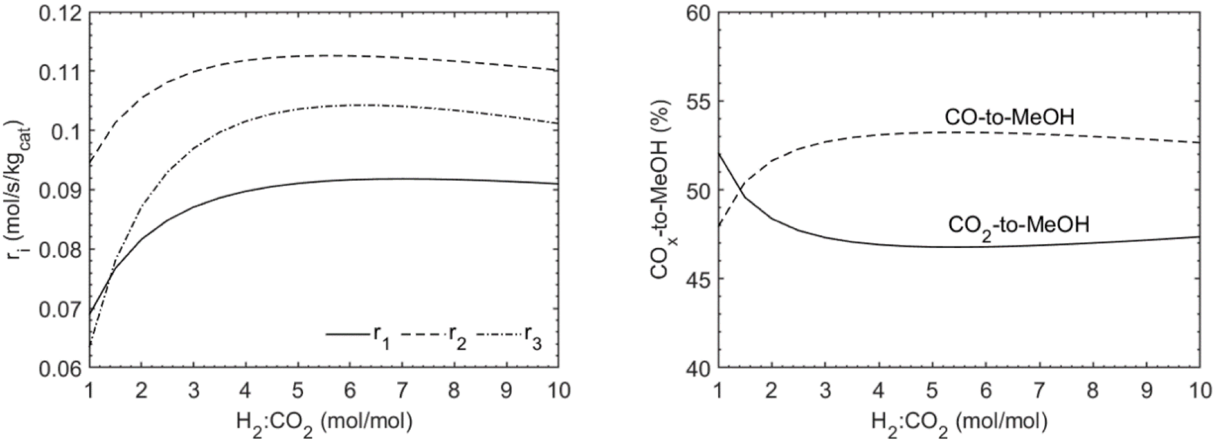

(a) (b)

Fig. 10. Reaction rates of the CuCeZr system as a function of the H_2:CO_2 molar ratio (a) and relative contribution of CO and CO_2 to the formation of methanol as a function of the H_2:CO_2 molar ratio on the CuCeZr catalyst (b). The results were obtained via simulations, at a temperature of 200 °C, a pressure of 30 bar, a H_2:CO_2 ratio of 3 and a GHSV of $2.15\cdot10^5$ $NL\cdot kg_{cat}^{-1}\cdot h^{-1}$.

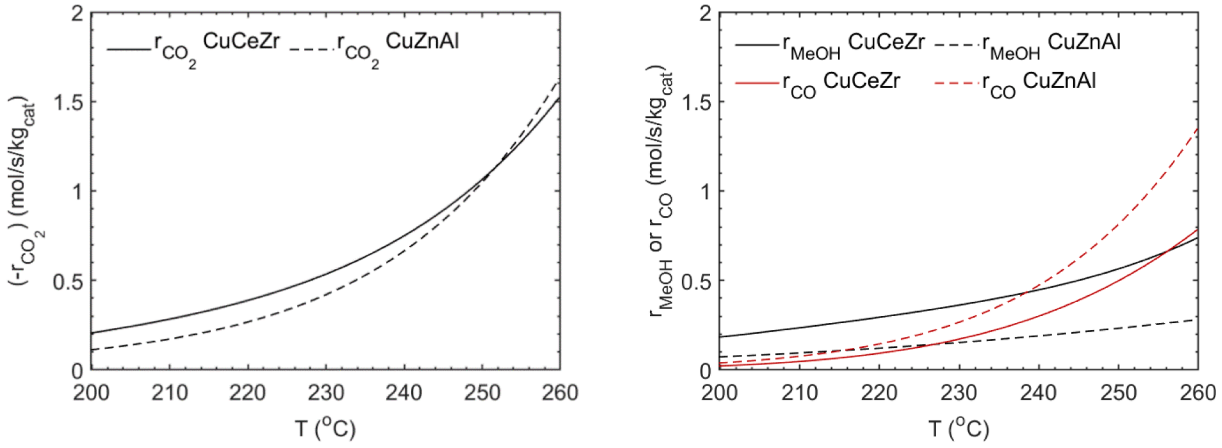

(a) (b)

Fig. 11. CO_2 consumption rate for the CuCeZr catalyst (solid line) and the CuZnAl catalyst (dashed line) as a function of temperature (a) and methanol and CO formation rate (black and red lines, respectively) for the CuCeZr catalyst (solid line) and the CuZnAl catalyst (dashed line). The results were obtained via simulations, at a pressure of 30 bar, a H_2:CO_2 ratio of 3 and a GHSV of $2.15 \cdot 10^5$ $NL \cdot kg_{cat}^{-1} \cdot h^{-1}$.

converts CO_2 more selectively to methanol – including both direct and indirect route – than the CuZnAl catalyst. As shown in Fig. 11**b**, methanol formation rate (r_{MeOH}) its higher for the CuCeZr and crosses with CO (r_{CO}) only at c.a. 256 °C. On the contrary, the CuZnAl shows a much faster production of CO than methanol over the entire temperature range, which indicates that the CO hydrogenation does not contribute significantly to the synthesis of methanol, being CO the main reaction product. This demonstrates that the CuCeZr catalyst allows for a delay in the selectivity decay with increasing temperature when compared to the benchmark. It is clear that, in principle, lower temperatures favour the methanol production over CO. On the contrary, a higher temperature would correspond to much faster reactions, requiring less amount of catalyst to achieve equilibrium. In the end, when the desired product – in this case methanol – comes from an exothermic reversible reaction, the choice of the optimal temperature lies on a trade-off between reaction performance and economics. However, it is clear that the CuCeZr would facilitate the conflict between the demand of high performance and catalyst/reactor costs, since it allows to achieve higher methanol selectivity and faster CO_2/CO conversion at higher temperature, when compared to the benchmark formulation.

6. Conclusions

In this work, we investigate the kinetics of the CO_2 conversion to methanol over a $Cu/CeO_2/ZrO_2$ catalyst, which remarkably outperforms the conventional $Cu/ZnO/Al_2O_3$ in terms of methanol yield/selectivity. The cross-over temperature (i.e., T_{cross}, defined as the temperature above which the yield to CO exceeds that of methanol) increases up to 240 °C for the CuCeZr, while CuZnAl shows a higher selectivity to CO in the entire temperature range.

We analyse in detail the one-site, dual-site and three adsorption sites kinetic models, based on hypothesis retrieved from literature, and accordingly derived the kinetic parameters of all the models via an optimization algorithm based on the minimization of the RMSE (root mean square error). Physicochemical constraints and statistical indicators were used as tool for model discrimination. The best performing kinetic model (i.e., dual-site model of Graaf et al.,) suggests that the reaction mechanism proceeds via the adsorption of one of the oxygens of CO_2 on the oxygen vacancies of the CeO_2-ZrO_2 phase (i.e., 1st active site), while H_2 adsorbs and dissociate on the metallic copper (i.e., 2nd active site). The adsorbed hydrogen preferentially hydrogenates the carbon atom giving rise to the formate route. According to this mechanism, methanol can be formed either directly from CO_2, or indirectly from the CO produced via the rWGS. The resulting kinetic model (i.e., rate expressions and fitted parameters) predicts the experimental data quite accurately, particularly the cross-over temperature (i.e., the model predicts that T_{cross} stabilizes at 258 °C at around H_2:CO_2 of c.a. 7.) Further, analysis of the individual reaction rates and the relative contributions of CO_2 and CO to the methanol synthesis (i.e., COx-to-MeOH) reveal that CO_2 and CO contribute evenly at 30 bar, H_2:CO_2 of 3 and 200 °C (i.e., 51.5% and 47.4%, respectively), while the pathway CO-to-MeOH takes over at higher temperatures and/or higher H_2 concentration. For H_2:CO_2 above 1.5, the CO contribution is predominant and exhibits an optimum at c.a. H_2:CO_2 of 7 (at 30 bar and 200 °C) , which likely corresponds to the saturation of the Cu^0 sites. This analysis underlines the importance of the indirect CO hydrogenation pathway in the reaction mechanism.

In conclusion, these findings lead to a deeper understanding of the reaction mechanism of CO_2 hydrogenation to methanol on novel CuCeZr systems, and serve as basis for future research into this catalyst formulation. For example, a more hydrophobic surface (i.e., weaker H_2O adsorption and faster desorption from Cu^0 sites) could lead to faster reaction rates and lower H_2 requirement in the feed. Furthermore catalyst modification that lead to stronger CO binding would facilitate CO hydrogenation and, thus increase the selectivity to methanol even at higher temperatures.

Declaration of Competing Interest

The authors declare that they have no known competing financial interests or personal relationships that could have appeared to influence the work reported in this paper.

Acknowledgements

This project has received funding from the European Union's Horizon 2020 research and innovation programme under grant agreement No 838014 (*C2Fuel* project).

Appendix A. Supplementary data

Supplementary data to this article can be found online at https://doi.org/10.1016/j.cej.2022.134946.

References

[1] E. Alper, O. Yuksel Orhan, CO2 utilization: developments in conversion processes, Petroleum 3 (1) (2017) 109–126.

[2] V. Ramanathan, Y. Feng, Air pollution, greenhouse gases and climate change: Global and regional perspectives, Atmos. Environ. 43 (1) (2009) 37–50.

[3] M.E. Boot-Handford, J.C. Abanades, E.J. Anthony, M.J. Blunt, S. Brandani, N. Mac Dowell, J.R. Fernández, M.-C. Ferrari, R. Gross, J.P. Hallett, R.S. Haszeldine, P. Heptonstall, A. Lyngfelt, Z. Makuch, E. Mangano, R.T.J. Porter, M. Pourkashanian, G.T. Rochelle, N. Shah, J.G. Yao, P.S. Fennell, Carbon capture and storage update, Energy Environ. Sci. 7 (1) (2014) 130–189.

[4] C. Cremer, M. Ball, M. Wietschel, Carbon Capture and Storage, in: M. Ball, M. Wietschel (Eds.), The Hydrogen Economy: Opportunities and Challenges, Cambridge University Press, Cambridge, 2009, pp. 168–198, https://doi.org/10.1017/CBO9780511635359.007.

[5] F. Sabatino, A. Grimm, F. Gallucci, M. van Sint Annaland, G.J. Kramer, M. Gazzani, A comparative energy and costs assessment and optimization for direct air capture technologies, Joule 5 (8) (2021) 2047–2076.

[6] A. Al-Mamoori, A. Krishnamurthy, A.A. Rownaghi, F. Rezaei, Carbon capture and utilization update, Energy Technology 5 (6) (2017) 834–849.

[7] F. Pontzen, W. Liebner, V. Gronemann, M. Rothaemel, B. Ahlers, CO2-based methanol and DME–Efficient technologies for industrial scale production, Catal. Today 171 (1) (2011) 242–250.

[8] M. Alvarado, The changing face of the global methanol industry, IHS Chemical Bulletin 3 (2016) 10–11.

[9] R. Singh, K. Tripathi, K.K. Pant, Investigating the role of oxygen vacancies and basic site density in tuning methanol selectivity over Cu/CeO2 catalyst during CO2 hydrogenation, Fuel 303 (2021) 121289, https://doi.org/10.1016/j.fuel.2021.121289.

[10] H.A. Zaidi, K.K. Pant, Catalytic conversion of methanol to gasoline range hydrocarbons, Catal. Today 96 (3) (2004) 155–160.

[11] C. Ortega, M. Rezaei, V. Hessel, G. Kolb, Methanol to dimethyl ether conversion over a ZSM-5 catalyst: Intrinsic kinetic study on an external recycle reactor, Chem. Eng. J. 347 (2018) 741–753.

[12] S. Ghosh, J. Sebastian, L. Olsson, D. Creaser, Experimental and kinetic modeling studies of methanol synthesis from CO2 hydrogenation using In2O3 catalyst, Chem. Eng. J. 416 (2021) 129120, https://doi.org/10.1016/j.cej.2021.129120.

[13] J.-F. Portha, K. Parkhomenko, K. Kobl, A.-C. Roger, S. Arab, J.-M. Commenge, L. Falk, Kinetics of methanol synthesis from carbon dioxide hydrogenation over copper–zinc oxide catalysts, Ind. Eng. Chem. Res. 56 (45) (2017) 13133–13145.

[14] G. Bozzano, F. Manenti, Efficient methanol synthesis: Perspectives, technologies and optimization strategies, Prog. Energy Combust. Sci. 56 (2016) 71–105.

[15] E. Fiedler G. Grossmann D.B. Kersebohm G. Weiss C. Witte Ullmann's Encyclopedia of Industrial Chemistry Wiley-VCH Verlag GmbH & Co. KGaA Weinheim, Germany 10.1002/14356007.a16_465.

[16] Y.-F. Zhao, Y. Yang, C. Mims, C.H.F. Peden, J. Li, D. Mei, Insight into methanol synthesis from CO2 hydrogenation on Cu (1 1 1): Complex reaction network and the effects of H2O, J. Catal. 281 (2) (2011) 199–211.

[17] R. Raudaskoski, E. Turpeinen, R. Lenkkeri, E. Pongrácz, R.L. Keiski, Catalytic activation of CO2: Use of secondary CO2 for the production of synthesis gas and for methanol synthesis over copper-based zirconia-containing catalysts, Catal. Today 144 (3-4) (2009) 318–323.

[18] S.G. Jadhav, P.D. Vaidya, B.M. Bhanage, J.B. Joshi, Catalytic carbon dioxide hydrogenation to methanol: a review of recent studies, Chem. Eng. Res. Des. 92 (11) (2014) 2557–2567.

[19] O. Tursunov, L. Kustov, A. Kustov, A brief review of carbon dioxide hydrogenation to methanol over copper and iron based catalysts, Oil & Gas Sciences and Technology-Revue d'IFP Energies nouvelles 72 (5) (2017) 30, https://doi.org/10.2516/ogst/2017027.

[20] C. Federsel, R. Jackstell, M. Beller, State-of-the-art catalysts for hydrogenation of carbon dioxide, Angew. Chem. Int. Ed. 49 (36) (2010) 6254–6257.

[21] R. Guil-López, N. Mota, J. Llorente, E. Millán, B. Pawelec, J.L.G. Fierro, R. M. Navarro, Methanol synthesis from CO2: a review of the latest developments in heterogeneous catalysis, Materials 12 (23) (2019) 3902, https://doi.org/10.3390/ma12233902.

[22] G. Bonura, F. Arena, G. Mezzatesta, C. Cannilla, L. Spadaro, F. Frusteri, Role of the ceria promoter and carrier on the functionality of Cu-based catalysts in the CO2-to-methanol hydrogenation reaction, Catal. Today 171 (1) (2011) 251–256.

[23] F. Arena, G. Mezzatesta, G. Zafarana, G. Trunfio, F. Frusteri, L. Spadaro, How oxide carriers control the catalytic functionality of the Cu–ZnO system in the hydrogenation of CO2 to methanol, Catal. Today 210 (2013) 39–46.

[24] X.-M. Liu, G.Q. Lu, Z.-F. Yan, J. Beltramini, Recent advances in catalysts for methanol synthesis via hydrogenation of CO and CO2, Ind. Eng. Chem. Res. 42 (25) (2003) 6518–6530.

[25] F. Arena, G. Italiano, K. Barbera, S. Bordiga, G. Bonura, L. Spadaro, F. Frusteri, Solid-state interactions, adsorption sites and functionality of Cu-ZnO/ZrO2 catalysts in the CO2 hydrogenation to CH3OH, Appl. Catal. A 350 (1) (2008) 16–23.

[26] A. Ateka, I. Sierra, J. Ereña, J. Bilbao, A.T. Aguayo, Performance of CuO–ZnO–ZrO2 and CuO–ZnO–MnO as metallic functions and SAPO-18 as acid function of the catalyst for the synthesis of DME co-feeding CO2, Fuel Process. Technol. 152 (2016) 34–45.

[27] G. Bonura, M. Cordaro, C. Cannilla, F. Arena, F. Frusteri, The changing nature of the active site of Cu-Zn-Zr catalysts for the CO2 hydrogenation reaction to methanol, Appl. Catal. B 152-153 (2014) 152–161.

[28] M. Lachowska, J. Skrzypek, Methanol synthesis from carbon dioxide and hydrogen over Mn-promoted copper/zinc/zirconia catalysts, React. Kinet. Catal. Lett. 83 (2) (2004) 269–273.

[29] K.T. Jung, A.T. Bell, Effects of zirconia phase on the synthesis of methanol over zirconia-supported copper, Catal. Lett. 80 (1) (2002) 63–68.

[30] K. Chang, T. Wang, J.G. Chen, Hydrogenation of CO2 to methanol over CuCeTiOx catalysts, Appl. Catal. B 206 (2017) 704–711.

[31] L. Lin, S. Yao, Z. Liu, F. Zhang, N.a. Li, D. Vovchok, A. Martínez-Arias, R. Castañeda, J. Lin, S.D. Senanayake, D. Su, D. Ma, J.A. Rodriguez, In situ characterization of Cu/CeO2 nanocatalysts for CO2 hydrogenation: morphological effects of nanostructured ceria on the catalytic activity, The Journal of Physical Chemistry C 122 (24) (2018) 12934–12943.

[32] B.i. Ouyang, W. Tan, B. Liu, Morphology effect of nanostructure ceria on the Cu/CeO2 catalysts for synthesis of methanol from CO2 hydrogenation, Catal. Commun. 95 (2017) 36–39.

[33] M. Konsolakis M. Lykaki S. Stefa S.A.C. Carabineiro G. Varvoutis E. Papista G.E. Marnellos CO2 Hydrogenation over Nanoceria-Supported Transition Metal Catalysts: Role of Ceria Morphology (Nanorods versus Nanocubes) and Active Phase Nature (Co versus Cu) Nanomaterials 9 12 1739 10.3390/nano9121739.

[34] L. Spadaro, A. Palella, F. Arena, Copper-Iron-Zinc-Cerium oxide compositions as most suitable catalytic materials for the synthesis of green fuels via CO2 hydrogenation, Catal. Today 379 (2021) 230–239.

[35] R.-W. Liu, Z.-Z. Qin, H.-B. Ji, T.-M. Su, Synthesis of dimethyl ether from CO2 and H2 using a Cu–Fe–Zr/HZSM-5 catalyst system, Ind. Eng. Chem. Res. 52 (47) (2013) 16648–16655.

[36] X. Zhou, T. Su, Y. Jiang, Z. Qin, H. Ji, Z. Guo, CuO-Fe2O3-CeO2/HZSM-5 bifunctional catalyst hydrogenated CO2 for enhanced dimethyl ether synthesis, Chem. Eng. Sci. 153 (2016) 10–20.

[37] L. Zhang, Y. Zhang, S. Chen, Effect of promoter SiO2, TiO2 or SiO2-TiO2 on the performance of CuO-ZnO-Al2O3 catalyst for methanol synthesis from CO2 hydrogenation, Appl. Catal. A 415-416 (2012) 118–123.

[38] J. Yu, M. Yang, J. Zhang, Q. Ge, A. Zimina, T. Pruessmann, L. Zheng, J.-D. Grunwaldt, J. Sun, Stabilizing Cu+ in Cu/SiO2 catalysts with a shattuckite-like structure boosts CO2 hydrogenation into methanol, ACS Catal. 10 (24) (2020) 14694–14706.

[39] H. Yang, P. Gao, C. Zhang, L. Zhong, X. Li, S. Wang, H. Wang, W. Wei, Y. Sun, Core–shell structured Cu@ m-SiO2 and Cu/ZnO@ m-SiO2 catalysts for methanol synthesis from CO2 hydrogenation, Catal. Commun. 84 (2016) 56–60.

[40] J. Graciani, K. Mudiyanselage, F. Xu, A.E. Baber, J. Evans, S.D. Senanayake, D. J. Stacchiola, P. Liu, J. Hrbek, J.F. Sanz, J.A. Rodriguez, Highly active copper-ceria and copper-ceria-titania catalysts for methanol synthesis from CO2, Science 345 (6196) (2014) 546–550.

[41] K.K. Bando, K. Sayama, H. Kusama, K. Okabe, H. Arakawa, In-situ FT-IR study on CO2 hydrogenation over Cu catalysts supported on SiO2, Al2O3, and TiO2, Appl. Catal. A 165 (1-2) (1997) 391–409.

[42] J. Xiao, D. Mao, X. Guo, J. Yu, Effect of TiO2, ZrO2, and TiO2–ZrO2 on the performance of CuO–ZnO catalyst for CO2 hydrogenation to methanol, Appl. Surf. Sci. 338 (2015) 146–153.

[43] C. Liu, X. Guo, Q. Guo, D. Mao, J. Yu, G. Lu, Methanol synthesis from CO2 hydrogenation over copper catalysts supported on MgO-modified TiO2, J. Mol. Catal. A: Chem. 425 (2016) 86–93.

[44] M. Epifani, T. Andreu, S. Abdollahzadeh-Ghom, J. Arbiol, J.R. Morante, Synthesis of ceria–zirconia nanocrystals with improved microstructural homogeneity and oxygen storage capacity by hydrolytic sol–gel process in coordinating environment, Adv. Funct. Mater. 22 (13) (2012) 2867–2875.

[45] D.H. Prasad, S.Y. Park, H.-I. Ji, H.-R. Kim, J.-W. Son, B.-K. Kim, H.-W. Lee, J.-H. Lee, Structural Characterization and Catalytic Activity of Ce 0.65 Zr 0.25 RE 0.1 O 2−δ Nanocrystalline Powders Synthesized by the Glycine-Nitrate Process, J. Phys. Chem. C 116 (5) (2012) 3467–3476.

[46] J.I. Gutiérrez-Ortiz, B. de Rivas, R. López-Fonseca, J.R. González-Velasco, Combustion of aliphatic C2 chlorohydrocarbons over ceria–zirconia mixed oxides catalysts, Appl. Catal. A 269 (1-2) (2004) 147–155.

[47] I. Atribak, F.E. López-Suárez, A. Bueno-López, A. García-García, New insights into the performance of ceria–zirconia mixed oxides as soot combustion catalysts. Identification of the role of "active oxygen" production, Catal. Today 176 (1) (2011) 404–408.

[48] M. Haneda, K. Shinoda, A. Nagane, O. Houshito, H. Takagi, Y. Nakahara, K. Hiroe, T. Fujitani, H. Hamada, Catalytic performance of rhodium supported on ceria–zirconia mixed oxides for reduction of NO by propene, J. Catal. 259 (2) (2008) 223–231.

[49] Z. Shi, Q. Tan, D. Wu, Ternary copper-cerium-zirconium mixed metal oxide catalyst for direct CO2 hydrogenation to methanol, Mater. Chem. Phys. 219 (2018) 263–272.

[50] W. Wang, Z. Qu, L. Song, Q. Fu, Probing into the multifunctional role of copper species and reaction pathway on copper-cerium-zirconium catalysts for CO2 hydrogenation to methanol using high pressure in situ DRIFTS, J. Catal. 382 (2020) 129–140.

[51] W. Wang, et al., "An investigation of Zr/Ce ratio influencing the catalytic performance of CuO/Ce1-xZrxO2 catalyst for CO2 hydrogenation to CH3OH." *Journal of Energy*, Chemistry 47 (2020) 18–28.

[52] A. Trovarelli, Structural and oxygen storage/release properties of CeO2-based solid solutions, Comments Inorg. Chem. 20 (4-6) (1999) 263–284.

[53] J.J. Meyer, P. Tan, A. Apfelbacher, R. Daschner, A. Hornung, Modeling of a methanol synthesis reactor for storage of renewable energy and conversion of CO2–comparison of two kinetic models, Chem. Eng. Technol. 39 (2) (2016) 233–245.

[54] T. Henkel, Modellierung von Reaktion und Stofftransport in geformten Katalysatoren am Beispiel der Methanolsynthese, Technische Universität München, Diss, 2011.

[55] F. Nestler, A.R. Schütze, M. Ouda, M.J. Hadrich, A. Schaadt, S. Bajohr, T. Kolb, Kinetic modelling of methanol synthesis over commercial catalysts: A critical assessment, Chem. Eng. J. 394 (2020) 124881, https://doi.org/10.1016/j.cej.2020.124881.

[56] C. Seidel, A. Jörke, B. Vollbrecht, A. Seidel-Morgenstern, A. Kienle, Kinetic modeling of methanol synthesis from renewable resources, Chem. Eng. Sci. 175 (2018) 130–138.

[57] T. Kubota, I. Hayakawa, H. Mabuse, K. Mori, K. Ushikoshi, T. Watanabe, M. Saito, Kinetic study of methanol synthesis from carbon dioxide and hydrogen, Appl. Organomet. Chem. 15 (2) (2001) 121–126.

[58] G.H. Graaf, E.J. Stamhuis, A.A.C.M. Beenackers, Kinetics of low-pressure methanol synthesis, Chem. Eng. Sci. 43 (12) (1988) 3185–3195.

[59] K.M.V. Bussche, G.F. Froment, A steady-state kinetic model for methanol synthesis and the water gas shift reaction on a commercial Cu/ZnO/Al2O3Catalyst, J. Catal. 161 (1) (1996) 1–10.

[60] G. Liu, et al., The role of CO2 in methanol synthesis on Cu Zn oxide: An isotope labeling study, J. Catal. 96 (1) (1985) 251–260.

[61] M. Bowker, et al., The mechanism of methanol synthesis on copper/zinc oxide/alumina catalysts, J. Catal. 109 (2) (1988) 263–273.

[62] Y. Yang, C.A. Mims, D.H. Mei, C.H.F. Peden, C.T. Campbell, Mechanistic studies of methanol synthesis over Cu from CO/CO2/H2/H2O mixtures: The source of C in methanol and the role of water, J. Catal. 298 (2013) 10–17.

[63] N.D. Nielsen, A.D. Jensen, J.M. Christensen, The roles of CO and CO2 in high pressure methanol synthesis over Cu-based catalysts, J. Catal. 393 (2021) 324–334.

[64] L.C. Grabow, M. Mavrikakis, Mechanism of methanol synthesis on Cu through CO2 and CO hydrogenation, ACS Catal. 1 (4) (2011) 365–384.

[65] N. Park, M.-J. Park, Y.-J. Lee, K.-S. Ha, K.-W. Jun, Kinetic modeling of methanol synthesis over commercial catalysts based on three-site adsorption, Fuel Process. Technol. 125 (2014) 139–147.

[66] Y. Slotboom, M.J. Bos, J. Pieper, V. Vrieswijk, B. Likozar, S.R.A. Kersten, D.W. F. Brilman, Critical assessment of steady-state kinetic models for the synthesis of methanol over an industrial Cu/ZnO/Al2O3 catalyst, Chem. Eng. J. 389 (2020) 124181, https://doi.org/10.1016/j.cej.2020.124181.

[67] C.V. Ovesen, B.S. Clausen, J. Schiøtz, P. Stoltze, H. Topsøe, J.K. Nørskov, Kinetic implications of dynamical changes in catalyst morphology during methanol synthesis over Cu/ZnO catalysts, J. Catal. 168 (2) (1997) 133–142.

[68] C.J.G. Van Der Grift, et al., Effect of the reduction treatment on the structure and reactivity of silica-supported copper particles, J. Catal. 131 (1) (1991) 178–189.

[69] J.C. Lagarias, et al., Convergence behavior of the Nelder-Mead simplex algorithm in low dimensions, SIAM J. Optimization 9 (1999) 112–147.

[70] D.E. Mears, Tests for transport limitations in experimental catalytic reactors, Ind. Eng. Chem. Process Des. Dev. 10 (4) (1971) 541–547.

[71] P.B. Weisz, C.D. Prater, “Interpretation of measurements in experimental catalysis.” *Advances in catalysis* Vol. 6 (1954) 143–196.

[72] G.H. Graaf, P.J.J.M. Sijtsema, E.J. Stamhuis, G.E.H. Joosten, Chemical equilibria in methanol synthesis, Chem. Eng. Sci. 41 (11) (1986) 2883–2890.

[73] O. Levenspiel, Chemical Reaction Engineering, Ind. Eng. Chem. Res. 38 (11) (1999) 4140–4143.

[74] I.b. Chorkendorff, J.W. Niemantsverdriet, Concepts of modern catalysis and kinetics, John Wiley & Sons, 2017.